University of Zurich[UZH]

Department of Physics
Faculty of Science

USZ Universitäts Spital Zürich

Radio-Oncology Clinic
Medical Physics Group

Patient-Specific Quality Assurance for Magnetic Resonance Guided Linear Accelerator

Department of Physics
Faculty of Science
Master Thesis

Michael Baumgartl
Dr. Stefanie Ehrbar
Dr. Stephanie Tanadini Lang
Prof. Dr. Jan Unkelbach

Author:	Yasaman Safarkhanlo
	yasaman.safarkhanlo@uzh.ch
Matriculation number:	18-746-859
Major:	Physics
Submission date:	30.12.2020

Abstract

Purpose: To evaluate the performance of the Delta^4 + MR phantom in a magnetic field of 0.345 T and give a general report on the early clinical experience of using the phantom for patient quality assurance. Also, to define some metrics to predict the complexity of the radiotherapy patient treatment plans.
Methods: The basic characteristics of the MR-compatible Delta^4 + MR phantom, like output stability, dose linearity, field size dependency, angular dependency, and planned versus delivered dose comparisons were examined. Additionally, patient-specific QA of 205 patient plans was performed and evaluated. Additionally, Modulation Complexity Score (MCS), Small Monitor Unit Score (SMUS), and Small Field Score (SFS) metrics were introduced and their relations with different plan features, such as the total number of monitor units, and gamma agreement index with two different criteria were investigated.
Results: The output stability, dose linearity, and field size dependency of the phantom were less than 2%. The average gamma passing rate for the detectors angular dependency and the first 205 patient plans (41 Prostate, 40 Lung, 26 Liver, 8 Head and Neck, and other sites) were above the 95% for 3%/3mm criteria. On the other hand, the metrics have no correlation with the gamma agreement indices and plan characteristics for the 153 delivered plans.
Conclusions: We found that the MR-compatible Delta^4+MR phantom is stable over time and shows only a small directional and field size dependence. Therefore, it was found to be safe and effective for use in the 0.345 T MRIdian MR-linac and can be used for patient-specific QA without concerns. However, the introduced complexity parameters could not predict the deliverability and accuracy of the treatment plans and other methods like machine learning are required to further investigate the difficulty of the treatment plans.

Dedication

A beautiful soul is never forgotten.

In loving memory of
Pouneh Gorji,
Arash Pourzarabi,
and all the 176 passengers of flight PS752.

Acknowledgments

With many thanks to all the USZ radiation oncology group for their energy, understanding, and help throughout my thesis, especially to my supervisors Michael Baumgartl, Dr. Stefanie Ehrbar, and Dr. Stephanie Tanadini-Lang for their guidance on the project, and Dr. Jan Unkelbach for his advice on the process. I would also like to thank Madalyne Chamberlain, Dr. Lotte Wilke, Dr. Mariangela Zamburlini, and Dr. Jerome Krayenbühl for their help on the MRIdian, phantoms, and the treatment planning systems. Thank you all for giving me an opportunity to learn from you during this time.

I am delighted to work alongside Michael Baumgartl, Dr. Stefanie Ehrbar, and Dr. Stephanie Tanadini-Lang because in addition to their scientific help, they were always ready to advise me on this thesis during day and night and helped me go through the hardest time of my life when I have lost my friends. This work could not have been carried out without your feedback in a very short amount of time on the days before submission.

And my biggest thanks go to my parents and my grandma for all the unconditional support you have shown me. My husband, Ali, thanks for your patience and encouragement, without which I could have never finished this project. You have been amazing, I will clean the living room from my papers now as I have promised you. To my sister, Samaneh, thank you for all these years being my best friend even remotely during this time and advising me on how to boost my mental health. And finally, my aunt, Sarvenaz, thanks for always being there when I needed help and guidance the most.

Contents

List of Figures

List of Tables

Acronyms

3-D Three-Dimensional. 10

3-D CRT Three-Dimensional Conformal Radiation Therapy. 4

AAPM American Association of Physicists in Medicine. 15

AAV Aperture Area Variability. 25

BED Biological Effective Dose. 2

CBCT Cone Beam CT. 6

CT Computed Tomography. 4, 10

CTV Clinical Target Volume. 5

DD Dose Difference. 19

DTA Distance to Agreement. 19

EBRT External Beam Radiation Therapy. 3

EPID Electronic Portal Imaging Device. 9

ERE Electron Return Effect. 10

FFF Flattening Filter-Free. 9

FID Free Induction Decay. 9

FOPH Federal Office of Public Health. 15

GAI Gamma Agreement Index. 19

GTV Gross Tumor Volume. 5

Gy Gray. 2, 17

HT Helical Tomotherapy. 4

IARC International Agency for Research on Cancer. 1

IC Ionization Chamber. 16

ICRU International Commission on Radiation Units and Measurements. 5

IGRT Image Guided Radiation Therapy. 6, 10

IMPT Intensity Modulated Proton Therapy. 5

IMRT Intensity Modulated Radiation Therapy. 4, 33

IR Ionizing Radiation. 1

ITV Internal Target Volume. 6

KERMA Kinetic Energy Released per unit MAss. 17

LET Linear Energy Transfer. 1

Linac Linear Accelerator. 4, 8, 33

LSV Leaf Sequence Variability. 25

MCS Modulation Complexity Score. 7, 25, 33

MLC Multi-Leaf Collimator. 9

MR Magnetic Resonance. 33

MR-linac Magnetic Resonance Guided Linear Accelerator. 6, 33

MRI Magnetic Resonance Imaging. 5, 8

MU Monitor Unit. 18

NTCP Normal Tissue Complication Probability. 3

OAR Organ at Risk. 4

PET Positron Emission Tomography. 5

PMMA PolyMethylMethAcrylate. 17

PRV Planning organ at Risk Volume. 6

PSPT Passively Scattered Proton Therapy. 5

PSQA Patient-Specific Quality Assurance. 15

PTV Planning Target Volume. 6

QA Quality Assurance. 5, 15, 33

R Relative Response. 18

RF Radio Frequency. 8

RT Radiation Therapy. 1, 15

SAD Source to Axis Distance. 11

SBRT Stereotactic Body Radiation Therapy. 4, 33

SDCF Suggested Daily Correction Factor. 18

SDD Source to Detector Distance. 11

SFS Small Field Score. 7, 26, 33

SID Source to Isocenter Distance. 13

SMUS Small Monitor Unit Score. 7, 26, 33

SRO Swiss Society for Radiation Oncology. 15

SSRMP Swiss Society of Radiobiology and Medical Physics. 15

SVMTRA Swiss Association of Specialists in Medical-technical Radiology. 15

TCP Tumor Control Probability. 3

TPS Treatment Planning System. 14, 18

VMAT Volumetric Modulated Arc Therapy. 4

Chapter 1

Introduction

As defined by the American Cancer Society, cancer is a group of diseases characterized by uncontrolled growth and spread of abnormal cells called malignant tumors [1]. International Agency for Research on Cancer (IARC) has identified cancer as one of the leading causes of death worldwide, around 9.9 million deaths in 2020.

The IARC has classified that the interaction between a person's genetic factors and carcinogens can cause cancer. A carcinogen is any factor that can promote carcinogenesis, the formation of cancer [2]. The main types of carcinogens are; 1. physical carcinogens, such as ionizing radiation, 2. chemical carcinogens, such as components of tobacco smoke, and 3. biological carcinogens, such as infections from certain viruses, bacteria, or parasites [3].

Physicians prescribe the required type of therapy for treating cancer based on cancer type, its advancement (stage at diagnosis), and the overall patient's health. A patient can receive only one type of treatment, but mostly they receive a combination of treatments, that is to say, surgery, chemotherapy, radiation therapy, immunotherapy, and others.

1.1 Radiation therapy

The main goal in radiation therapy (RT) is to kill the tumor cells using ionizing radiation (IR) such as electromagnetic waves, x- or γ-ray, and ionizing particles like electrons, neutrons, and protons [4]. For characterizing the quality of IR, the average energy deposited by an ionized particle to the medium per unit distance called linear energy transfer (LET) is introduced [5]. When an ion passes across the medium, it loses energy, therefore its LET increases, also for the same ion energy, LET increases with the ion size. LET value start from 1 keV/μm (low-LET: χ, γ-rays) to 10 keV/μm for radiation therapy protons, 10 - 100 keV/μm for carbon ions, and even higher values (more than 100 keV/μm) for alpha-particles or heavy charged particles, like space radiation [6] [7] [8].

Ionizing radiations only interact with the atoms, and the consequence of these interactions with the atomic structure of the cells is their biological effect on them. The direct effect of IR is when the radiation interacts with atoms of a DNA molecule or other cellular components which are critical for the survival of the cell, affecting its ability to reproduce and survive. Direct interaction with the cell's life-sustaining system can destroy it if enough atoms get damaged, and the chromosomes do not replicate correctly or the DNA information changes significantly. However, since critical components of the cell, such as DNA, takes only a small part of it, the probability of direct interaction with ionizing radiation is very low. On the contrary, considering that most of the human body is water, the odds of radiation interacting with water and producing hydrogen (H) and hydroxyls (OH) is high. These components may recombine or interact with other ions or fragments and form harmless compounds, but they could also create toxic substances, like hydrogen

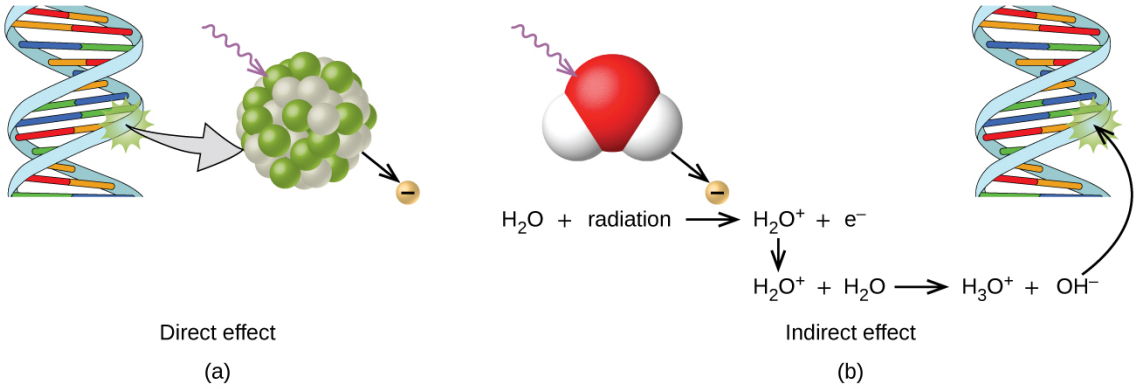

Figure 1.1: Ionizing radiation effects. Direct ionization is known as direct because the interaction occurs directly between a particle and a cellular component without an intermediary step. Indirect ionization effect is called indirect because of the intermediate step of H2O-based free radical formation (Image courtesy of OpenStax) [4].

peroxide (H_2O_2), which can destruct the cell. The later is the indirect effect of the IR on the living cells. Figure 1.1 shows the direct and indirect effects of the IR [4].

Radiation therapy's principle is trying to minimize the exposure of healthy cells to the radiation and maximize the delivered dose to cancer cells. Thus, cell survival and the shape of cell survival curves play a crucial role in radiotherapy. The relationship between cell survival, S, and cell killing can generally be explained by a linear-quadratic model in (1.1.1), where D is the delivered dose. The absorbed dose, or simply dose, is the mean energy absorbed per mass by ionizing radiation and it is measured in one Joule of energy absorbed per kilogram of mass called gray (Gy). The term α gives the initial slope of the curve while β is responsible for the bending of the curve as the dose increases. For large α/β ratios, the curve is exponential without a shoulder. Whereas for small α/β values, there is a shoulder with an over-exponential decrease in survival fraction.

$$S = e^{-\alpha * D - \beta * D^2} \tag{1.1.1}$$

Figure 1.2 shows the survival fraction as a function of dose on a semi-logarithmic scale. For sparsely ionizing radiation with lower LET, such as X-rays, in low doses, the curve represents a straight exponential behavior. As dose increases, the curve bends until, at very high doses, it behaves exponentially again. On the other hand, densely ionizing radiation with higher LET, like α-particles, behaves approximately like an exponential function of dose from the origin [9].

Often, normal cells have a lower α/β ratio than tumor cells which concerning the survival curve, have a more bent curve. This means healthy tissue encompasses better repair mechanisms than tumor cells. This benefit can be obtained by dividing the treatment into multiple fractions. The biological effective dose (BED) is defined as the true biological dose delivered by a particular combination of dose per fraction and total dose to a particular tissue characterized by a specific α/β ratio. If n refers to the number of fractions and d to the fraction dose, one can show that:

$$BED = nd * (1 + \frac{d}{\alpha/\beta}) \tag{1.1.2}$$

Controlling cancer growth is one of RT's key advantages. Shrinking the size of the tumor and making surgery possible, being able to have a daily life beside the therapy, and controlling the pain are other plus points of radiotherapy. On the other hand, tiredness, sickness, and loss of organ function as a result of the delivered dose exceeding their tolerance rate are some examples of RT's possible side effects.

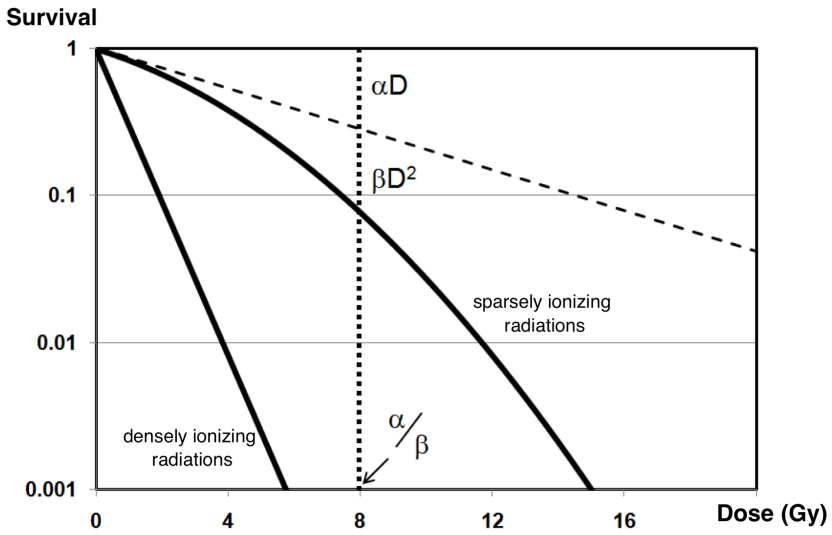

Figure 1.2: The linear-quadratic model of survival curve. The fraction of cells surviving is plotted on a logarithmic scale against dose on a linear scale. The ratio α/β is the dose where the linear and quadratic components are equal. Adapted from Hall [9].

The biological impact of the radiation on human tissue is categorized into deterministic and stochastic effects. Deterministic, also known as non-stochastic, effects are attributed to radiation effects that typically occur above a certain dose threshold. These effects depend on the time of exposure, doses, and type of radiation which their dependence is related to tumor control probability (TCP) and normal tissue complication probability (NTCP). These curves in figure 1.3 are usually sigmoidal and have a threshold, below which the deterministic effect does not exist. The slope and the D_{50} values are used to characterize the curves. D_{50} is the dose in which a probability of 50% is produced.

For reaching the goal of RT, every tumor has to be eradicated while at the same time the healthy tissues are spared. This means, TCP is to be maximized and NTCP is to be minimized. As in figure 1.3 shows, due to the steepness of the curves, a small uncertainty in the dose causes a huge change in the probabilities. The probability of uncomplicated tumor control, P^+, i.e. the probability of controlling the tumor without causing normal tissue complications, can be formulated by equation (1.1.3). The dose D_{opt}, which maximized P^+, can be considered the optimal dose if TCP and NTCP are equally important.

$$P^+ = TCP * (1 - NTCP) \tag{1.1.3}$$

Stochastic effects are biological effects which are randomly given and have no threshold. These effects have an increased probability of occurrence with increasing dose.

Patients can receive ionization radiation with various methods. Brachytherapy or internal radiation therapy is a method of RT using a sealed radiation source positioned near or directly within the targeted area (tumor). It applies high doses of radiation to a small area while sparing the surrounding healthy tissue. The brain, head and neck, lung, breast, prostate, and any type of cancer in which a radiation seed can be placed near the tumor can be treated with this technique. On the contrary, external beam radiation therapy (EBRT) is a method of RT when the radiation comes from a radiation source outside of the patient. This method can be used as a treatment method for almost every type of tumor site.

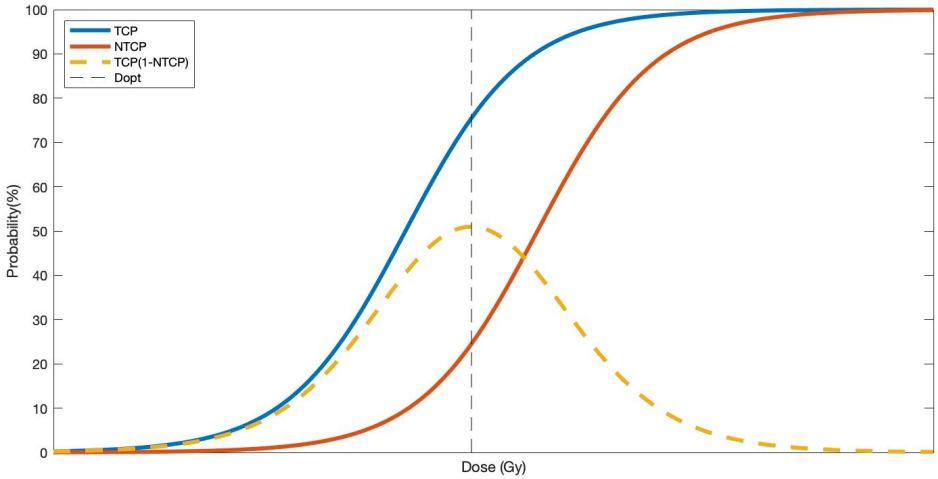

Figure 1.3: Dose-response curve for tumour control probability (TCP) and normal tissue complication probability (NTCP). The maximum probability for tumour control without normal tissue complications (dashed line) is reached at the optimum dose (D_{opt}) [10].

Patient's cancer type, their general health and medical history, the size and location of their tumor, its adjacency to normal tissues, the involvement of other types of cancer treatment like surgery or chemotherapy, and other factors like age, medical condition, and patient's preference plays a role in physician decision for choosing the right RT method.

1.2 External beam radiation therapy

External beam radiation therapy is one of the most common types of cancer therapy. It delivers high radiation dose directly into the target area, from a distant source placed in a machine outside the patient's body. Linear accelerators (Linac), cobalt-60 machines, and proton beam machines are some of the systems producing different types of radiation for EBRT. Radiation in EBRT is generated from accelerated particles used in these machines like electrons, protons, and some ions or sometimes a combination of them. These particles are either directly used to treat the tumor or they hit a target, where neutrons or photons are produced.

The main point of using EBRT instead of brachytherapy is to kill or eliminate the return of tumor cells using high radiation doses without an invasive operation for placing radioactive sources inside the patient's body. It is a painless and non-invasive procedure with a lower risk compared to the other cancer treatments. Contrarily, EBRT has some downsides like fatigue and irritation in the target areas.

The type of EBRT is defined by the radiation source and planning method being used for each treatment. Three-dimensional conformal radiation therapy (3-D CRT), intensity modulated radiation therapy (IMRT), and stereotactic body radiation therapy (SBRT) are some types of external beam radiation therapy. Three-dimensional CRT is a common type of EBRT which delivers conformal radiation beams from different directions to the target area and minimize the damage to the surrounding normal tissues. The precise location of the tumor and the Organs at Risk (OAR) are mapped out with computed tomography (CT) scans.

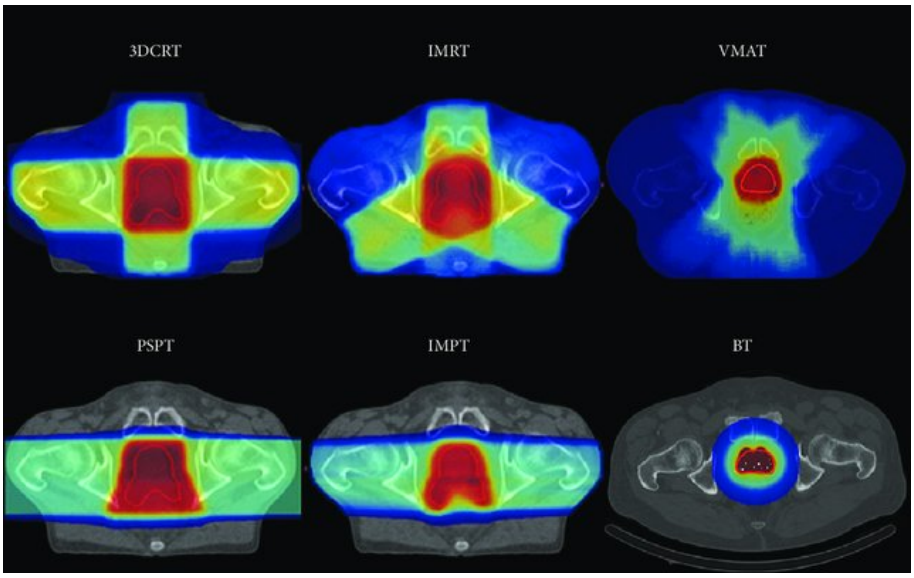

Figure 1.4: Different EBRT plans for the same patient. The red surface represents the high-dose regions, the yellow surface the intermediate-high-dose regions, the dark blue surface the low-dose regions, and the azure blue surface the intermediate-dose regions. The BT plan is presented for a comparison [11]

By optimizing the beam intensity, higher doses can be delivered to some areas of the tumor and reduce the dose transferred to normal cells. Radiation beams are divided into tiny beams (beamlets) that vary in dose, shape, and entry point. This highly accurate and curative treatment method is known as intensity modulated radiation therapy. Volumetric modulated arc therapy (VMAT) and helical tomotherapy (HT) that continuously deliver radiation as the machine rotates around the patient's body are special types of IMRT. Stereotactic body radiation therapy precisely delivers very high radiation doses to a tight tumor margin over a few treatment sessions with a combination of many small radiation fields. The application of SBRT is for treating small cancers in the body, including small lung or liver cancers or small metastases (cancer that has spread away from primary cancer). There are also other types of EBRT like passively scattered proton therapy (PSPT) and intensity modulated proton therapy (IMPT) which proton is their source of radiation. Figure 1.4 illustrates examples of dose distribution for treatment plans with different modalities calculated for the same patient [11].

When a patient is diagnosed with cancer, a CT scan is performed to locate the tumor and its position relative to other organs. Sometimes another imaging modality, such as magnetic resonance imaging (MRI) or positron emission tomography (PET), is used to register the CT image and the precise location of the tumor. When the tumor volume and the organs at risk are delineated, the physician gives a prescription dose and normal tissue dose constraints for creating a radiotherapy treatment plan. The treatment planner chooses the incident beam directions and determines the radiation fields. The treatment planning system calculates the final dose for each radiation field and optimizes the plan for the best possible irradiation beams. When the planner calculates the final dose distribution, the physician reviews the plan, and if everything was fine, approves it. After performing some quality assurance (QA) tests and dose measurement, the treatment starts.

Before the treatment begins, for improving the delivery accuracy of the radiotherapy treatment, the patient needs to be positioned relative to the treatment beams. X-ray imaging, fixation devices, and machine's lasers are used to position the patient in order to minimize any type of variations and fix the location of the target area.

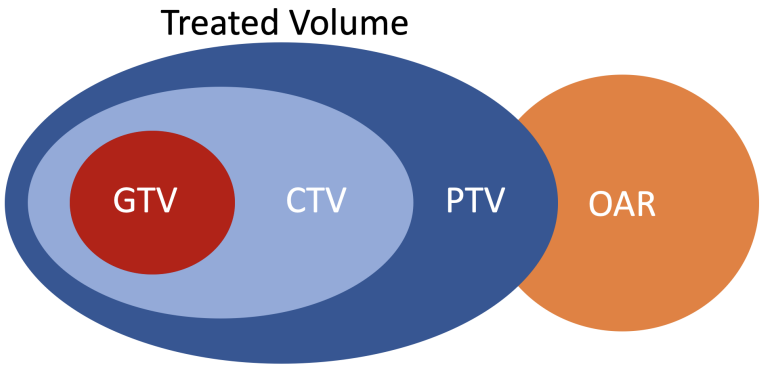

Figure 1.5: Schematic of the main RT planning volumes and organ at risk (OAR) located in the irradiated patient volume, taken from ICRU Report 50 [12][15].

1.3 Image guided radiation therapy

Imaging has three particular applications in radiation therapy. It makes accurate target delineation possible in treatment planning and manages the motion variations to localize and deliver the radiation. Also, during or after treatment, images are taken to evaluate and adapt the plans for the next treatments. Another application of imaging is the response assessment during the follow-ups.

Gross tumor volume (GTV) and clinical target volume (CTV), defined by the International Commission on Radiation Units and Measurements (ICRU) in Report 50, are two main concepts to be considered in radiation therapy planning. As illustrated in figure 1.5, GTV margins around the primary tumor. The CTV covers both the GTV and the extend of microscopic, un-imageable tumor spread around it [12]. When the planning target volume (PTV) margin gets smaller, fewer healthy cells will get irradiated, and the target area can receive more dose. That is why higher quality images are taken to define these margins more precisely.

Minimizing treatment uncertainties, like placement errors and geometric variation of the target and critical organs, is another issue in radiation therapy [13]. Hence, PTV is defined as a margin around the CTV to cover uncertainties in planning and delivery and consider the normal tissue structures around the target. In ICRU Report 62 in 1999, PTV was modified and the report incorporated more detail on the organs at risk to add a margin of uncertainty around them, if necessary, to create a planning organ at risk (PRV) [14] [12].

Variations in radiotherapy are either inter-fraction changes, which are the changes inside the patient from one treatment session to the next, or intra-fraction motions, which occur within a treatment delivery session. The PTV margin is applied to make room for daily set-up variations of the patient, and the internal target volume (ITV) is for the internal motions of the patient anatomy. After patient fixations with the marks and laser beams, better positioning and alignment is achieved with pre-treatment imaging. By using regular imaging, positioning errors reduce, and thus the size of the PTV and ITV margins decrease. While the CTV is being irradiated safely, and the overall therapy result gets significantly improved with reduced side effects.

Image guided radiation therapy (IGRT) is the radiotherapy method in which imaging modalities are applied before and during each treatment. They are used for positioning, adaptation, and motion tracking and improve the dose delivery precision to the target area. But this method requires expensive investments for the machine and its required infrastructure. It also adds some additional steps to the treatment process for the imaging.

The imaging modalities available for IGRT are planar X-ray imaging, X-ray CT, cone beam CT (CBCT), ultrasound, and MRI. They mostly use ionizing radiation for constructing an image and deliver an extra dose to the patient, except ultrasound and MRI.

Magnetic resonance imaging is non-ionizing and uses the magnetic properties of certain atomic nuclei, using radio-frequency instead of ionizing radiation to construct an image of the internal anatomy. The MRI guidance for external beam radiation therapy is being used in magnetic resonance guided linear accelerator (MR-linac). The MR-linac is a combination of two technologies - an MR scanner and linear accelerator – allowing better precision in locating tumors and delivering doses of radiation to the moving tumors.

1.4 Thesis motivation and outline

The motivations behind this work were to test the new MR-compatible Delta^4 + MR phantom and evaluate a method to determine which treatment plan requires an MR-linac patient-specific QA with this phantom. Chapter 2 details the theory behind MR-linac and patient-specific QA systems. This chapter explains the basics of MRI, linear accelerator, and patient-specific QA measurements and also describes the existing MR-linac and MR-compatible patient-specific QA systems. In chapter 3, the evaluation of the Delta^4 + MR phantom and its early clinical experience are presented. The tests performed for the phantom are daily output stability, dose linearity, field size dependency, angular dependency, and planned versus delivered dose comparison on the 0.345 T superconducting MR-linac. The modulation complexity score (MCS), small monitor unit score (SMUS), and small field score (SFS) introduced in chapter 4 evaluate the complexity of treatment plans in terms of field variability and contributions of small field areas and numbers of MU and characterize treatment sites based on these metrics. To determine whether independent 'new' information can be obtained from the metrics, their correlation with some plan features was calculated. Also, metric correlations with the Delta^4 + MR phantom gamma passing rates were measured to determine if any of them would correlate with dose accuracy of the delivered treatment plan. Finally, chapter 5 addresses the overall result of the phantom and metrics tests and presents an outlook for this work.

Chapter 2

Theory

Magnetic resonance imaging (MRI) is one of the main clinical imaging modalities. It uses non-ionizing radiation, providing excellent soft-tissue contrast, and acquiring multi-dimensional image information. It generates slice images of the human body in any selected direction or of any three-dimensional volume of the body based on the magnetic properties of hydrogen nuclei. Another unique feature of the MRI is measuring biological functions and physiology with functional imaging modalities. On the downside, MRI is much pricier than CT, has a higher image acquisition time, and because of its magnets, many patients with metallic implants get excluded from this modality[16]. Curran and his team introduced the first use of MRI in radiotherapy in the mid-1980s [17]. Since then, the application of MRI in RT has grown remarkably, and today, one of its most current applications in radiotherapy is MR-linac, which allows imaging during treatment.

2.1 Magnetic Resonance Guided Linear Accelerator

The MR-linac has brought an MR scanner and linear accelerator (Linac) together, realizing the idea of having a non-ionizing high-quality image of soft-tissue contrast in the target area for image guidance and plan adaptation before the irradiation [18] [19]. This daily adaption is only beneficial if it's combined with a highly conformal delivery technique such as IMRT or SBRT to optimally spare the healthy tissue.

2.1.1 Basic principles - MRI

The MRI is based on the directional magnetic field or moment, which is associated with charged particles in motion. Since the nuclei are charged particles with an odd number of protons and/or neutrons, they produce a minor magnetic moment when they precess. The human body is water abundant, a molecule that has a high gyromagnetic ratio. When the patient is placed in an MRI, the free hydrogen nuclei align themselves with the direction of the magnetic field and precess about the magnetic field direction like gyroscopes. This motion is called Larmor precession with the frequency proportional to the applied magnetic field strength characterized as the Larmor frequency, ω_0. The Larmor frequency is defined by equation (2.1.1) where γ is the gyromagnetic ratio, a nuclei specific constant, and B_0, the strength of the applied magnetic field. Larmor frequency is also known as 'resonance' frequency.

$$\omega_0 = \gamma B_0 \tag{2.1.1}$$

When a net magnetic moment, M, parallel to B_0 is created, a radio frequency (RF) pulse transmitted from an RF coil is applied to shift the M away from the B_0, the nuclei absorb the RF energy and go to an excited state. This RF pulse is perpendicular to B_0

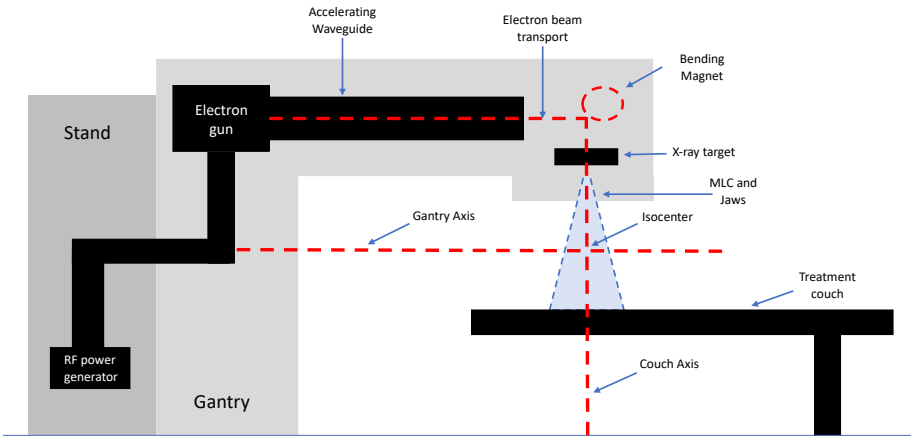

Figure 2.1: Schematic diagram of Linac treatment system

and equal to the ω_0. When the signal is turned off, the nuclei lose energy and go back to their equilibrium state with emitting an RF pulse, called free induction decay (FID) response signal, realigning their net magnetic moment with B_0. This step is known as the relaxation process. The FID signal is received by another set of RF coils and is used to obtain three-dimensional gray-scale MR images [16].

The time it takes for nuclei to go back to equilibrium is determined by two factors, T_1- and T_2-relaxation time. T_1 recovery or longitudinal relaxation only affects the magnetization in the z-component, and the T_2 decay or transverse relaxation affects the x- and y-directions. The inhomogeneities in the B_0 magnetic field alters the transverse magnetization. The T_2* decay quantifies this change.

2.1.2 Basic principles - Linac

The clinical linear accelerator is the entire treatment delivery system, including a rotating gantry, used in external beam radiation therapy. Linac's main gantry components are an RF power source, electron gun, accelerator guide, heavy metal source, and collimators shown in figure 2.1.

The electron gun sends electron pulses through the accelerator waveguide with specific time, velocity, and position to maximize the acceleration, and it is accelerated by the high-frequency electromagnetic waves supplied by the RF power source. The bending magnet guides the electron beam toward the patient, and when they collide with the heavy metal source, they produce Bremsstrahlung high-energy photon beams.

The rectangular field (jaws) and multileaf collimators (MLC), placed in the head of the gantry, shape the photon rays conforming to the target area leading to a non-homogeneous divergent photon field. The flattening filter creates a homogeneous photon field by attenuating the center more than the beam's sides. However, the attenuation by the shape and consistency of the filter reduces the dose rate.

The modern linacs usually have a flattening filter-free (FFF) design allowing high dose rate treatments. IMRT controls the dose intensity with the MLC creating a conformal and homogeneous total dose distribution, and since the energy spectrum is almost constant, the dose calculation is more straightforward.

A room-based laser, moving treatment couch, and imaging systems either mounted on the gantry or in the treatment room guarantee the high-precision patient setup using IGRT. Also, the electronic portal imaging device (EPID) placed on the linac can verify the patient's position. The target area is usually at the isocenter of the linac. Finally, the gantry rotates around the patient and delivers the treatment from various angles.

2.1.3 Motivation - MR-linac

The image guided radiation therapy (IGRT) minimizes uncertainties about the tumor's shape and location and reduces the delivered toxicities to the healthy tissues. Therefore, a high resolution, high-contrast image from the tumor and its surrounding normal tissues is acquired to provide an accurate tumor delineation.

The computed tomography (CT) images illustrate electron density and the patient's spatial position. It has been and still is one of the main pillars in three-dimensional (3-D) RT planning. Nevertheless, inadequate soft tissue contrast in CT and the necessity of imaging during treatment bring up the idea of including MRI multimodality imaging in RT [20]. This transition from the bony structure CT to high quality soft tissue and real time MRI poses new challenges.

The main challenge for combining an MR system with a linac is the effects of these two systems on each other. The proximity of the magnet to the linac can compromise the system's components functionality, and the Lorentz force applied to the charged particles deflect the pathway, causing the loss of beam current and a change in the dose distribution [21]. The shielding of the magnet or hardware can control this effect via creating a near zero Gauss region. The electron return effect (ERE) is another matter of concern for the MR-linac [22]. The secondary electrons bend their path in a circle away from the magnetic field, widen the beam penumbra and disrupt the symmetry of dose distribution. The radiation field size, magnetic field strength, and surface orientation have different impacts on this effect. With the help of Monte Carlo dose calculations, the opposing beams [22] and the multi-beam IMRT [23] can entirely cancel the electron return effect. Additionally, inverse treatment planning will mitigate this effect by considering the presence of the magnetic field. As the magnet strength increases, MLC engine performance weakens as a result of the Lorentz force [24]. An approach to minimize this effect is by replacing standard linac MLC with the redesigned MR-compatible components, but the efficient alternative can be decreasing the field strength. The homogeneity disruption of the main magnetic field (B_0) by the MLC is another challenge in designing an MR-linac. Changing the field with gradient or coils within the scanner manages this effect for the volume of interest with the process called active shimming [25]. Also, the passage of incident beams through the RF receiver coils leads to dose attenuation and an increase of skin dose via secondary electrons. The radiation induced current created by the beams makes interference and image artifacts [26]. The MR-compatible radiotranslucent [27] or radiotransparent [28] RF coils are the solutions for this issue [29].

Besides these technical challenges, the planning of the facilities and new safety issues, like quality control procedures and standards for both the MRI and radiation, has to be considered. The high capital and operational costs is another barrier that is preventing the MR-linacs to become widely used around the world [20].

The MRI's superiority offers an ability to enhance the accuracy of the irradiated target volume and organs at risk. As a result, visualizing difficult-to-image targets and critical structures becomes simpler and the plan adaptation improves, which primarily enhances the GTV. The possibility of 2D and 3D real-time imaging during the treatment is another benefit of integrating an MRI into a linac. In addition, due to the physics behind the MRI image acquisition, the patient does not receive an additional dose and more frequent imaging assessments can be done to track the anatomical response of the tumor and its surrounding tissue.

MR-linac is either constructed in the perpendicular configuration where the radiation is orthogonal or inline, where the beam is parallel to the magnetic field, as represented in figure 2.2.

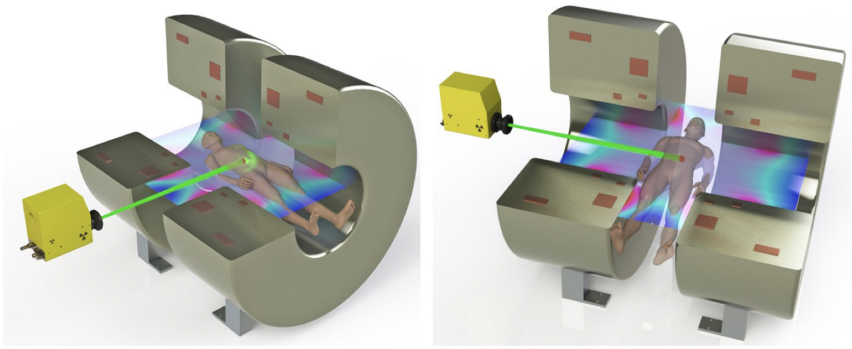

Figure 2.2: MR-linac configurations. MRI-linac systems are in either the perpendicular configuration, or the in-line configuration. The images shown here are based on the Australian prototype system, which was designed to facilitate operation in both configurations [30].

System commercial name	Beam strength	Field strength	Superconductor magnet type	Orientation
Elekta Unity	7 MV	1.5 T	Closed	Perpendicular
Australian MR-linac	4 and 6 MV	1.0 T	Open	Both
Aurora-RT MagnetTx	6 MV	0.6 T	Biplanar	Inline
ViewRay MRIdian	6 MV	0.35 T	Split	Perpendicular

Table 2.1: The current in development MR-linac systems in order of magnetic field strength [29]

2.1.4 Existing MR-linac systems

At the time of writing, Elekta Unity (Elekta AB, Stockholm, Sweden) [31] and ViewRay MRIdian (ViewRay Technologies Inc, Oakwood Village, Ohio) [32] are the two commercially available MR-linacs. There are at least two other systems in development, the Australian prototype [33] and the Aurora-RT system (MagnetTx Oncology Solutions, Edmonton, Alberta, Canada) [34]. The table 2.1 represents each one of these systems in order of magnetic field strength with their unique features.

Elekta Unity

Elekta AB (Stockholm, Sweden) and Philips (Best, the Netherlands) in collaboration with the University Medical Center Utrecht (Utrecht, the Netherlands) have integrated a modified 1.5 T Achieva Philips MRI and an Elekta 6 MV accelerator creating the Elekta Unity MR-linac system [35].

The latest design is an Elekta 7 MV FFF standing wave linac (Elekta, Crawley, UK) with a ring-based gantry containing a 1.5 T MRI system (Philips Ingenia, Best, The Netherlands), which are magnetically decoupled by the modified MRI active shielding. The shield creates a zero-field zone in the transversal midplane to minimize the magnetic interference at the accelerator tube [36] [37]. The linac is placed outside of the Faraday cage that manages the RF interference between the accelerator's components and the MRI system. This system rotates in either direction with its ring-mounted linac in a closed bore. The system has a 143.5 cm source to axis distance (SAD) from the target inside the 1.0 m radius MRI bore [38]. Figure 2.4 illustrates the sketch of this system.

The radiation beam passes through the magnet cryostat perpendicular to the field. The magnet's central region is split in two and has no gradient coils and shimming hardware in the longitudinal direction to reduce beam attenuation and conduct a homogeneous, circumferential beam transmission towards the isocenter [39]. The non-rotational 80 MLC pairs collimate the radiation beams with a 250 cGy/min dose rate at 1.0 m SAD. The MLC leaves are 0.72 cm wide at the isocenter plane with the maximum field size of 22 cm in feet-head and 57 cm in the lateral direction [31] [37].

(a) The Elekta Unity

(b) The Australian MRI-linac

(c) The Aurora-RT MagnetTx

(d) ViewRay MRIdian

Figure 2.3: Existing MR-linac systems. (a) Elekta's 1.5 T Unity system at University Medical Centre in Utrecht, The Netherlands. This was the MRI-linac used for the first in man treatments in May 2017 (courtesy of Elekta Unity). (b) The Australian MRI-linac. The treatment beam can be orientated either inline or perpendicular to the magnet bore (courtesy of ACRF Image X Institute). (c) Illustration of the Aurora-RT system (courtesy of MagnetTx Oncology Solutions). (d) The MRIdian system at University Hospital of Zurich.

Australian MR-linac

The Ingham Institute's Australian MR-linac has a 1.0 T open-bore magnet with 4 and 6 MV linac. It is the first inline and the only other high-field magnetic field system currently in the second stage of development. The device has both the inline and the perpendicular configuration, which is a versatile design for radiation beam entry and patient positioning. The beam enters the system parallel to the magnetic field in the machine's latest model. This system has an 82 cm diameter magnet with a 15 cm gap. The linac and MLC are in the low-field region along with the B_0, where the magnet is actively shielded. The 120 MLC leaves allow real-time treatment planning control. The linac is uniquely mounted on rails, providing different source-to-isocenter distances (SID), which enable dosimetric measurements at different magnetic field strengths [33].

Aurora-RT MagnetTx

The 0.6 T biplanar MRI system coupled with a 6 MV linac is the Aurora-RT MagnetTx system of the University of Alberta, Edmonton. The first configuration consisted of a 0.2 T MRI system, which was redesigned into a 0.5 T bi-planar MRI system on a transverse plane, and the linac mounted on the isocenter rotating with the MRI system. The magnet is passively shielded and has a 27.9 cm pole-to-pole gap, which minimizes the magnetic interference and allows the beam to transmit from the accelerator positioned laterally to the MRI. Both MR-linac configurations are possible with this design, but in the current model, the radiation beam entry is parallel to the magnetic field.

There are two dosimetry focal points in the design worth mentioning. The system can be switched on and off rather quickly with the high temperature superconducting magnet design, which enables zero field measurements. The electron contamination is reduced by an iron yoke inside the bore, which has restricted the border of the magnetic field [34].

ViewRay MRIdian

The ViewRay MRIdian MR-linac is a 6 MV FFF photon beam linear accelerator with a 0.345 T split superconducting magnet and a dose rate of 600 cGy/min. It is an advanced RT device with integrated components like treatment planning system (TPS) software, RT delivery system, and MRI scanner [40].

The initial design had a robotic 3-headed ^{60}Co system with a dose rate of 550 cGy/min [32] and is now replaced by a linac but keeping the overall MRI unit unchanged. The MRI system is a double-donut magnet that is connected mechanically and thermally with a 28 cm gap between the halves [41]. The linac components are assembled in a circular gantry at this gap, allowing the beam to emit perpendicular to the static magnetic field [29]. The gantry can be positioned at any angle except the degrees between 30°and 33°due to the technical limitations. The system has a low strength magnet that offers sufficient image quality for guidance, and at the same time, minimizes interactions between the linac and the MRI.

The linac has a 90 cm SAD and is equipped with 138 leaf pairs of double stacked and double focused MLC without additional jaws. The total MLC leaf height is 11 cm, with each stack's physical height amounts to 5.5 cm without any tongues or grooves. Stacks are shifted against each other by half a leaf width to minimize the radiation leakage. The effective leaf width is 4.15 mm with a single leaf width of 8.3 mm at the isocenter. The minimum field size of 0.2×0.415 cm^2 and the maximum field size of 27.4×24.1 cm^2 can be programmed with this system [32]. The linac is equipped with 138 leaf pairs of double stacked and double focused MLC [42]. For positioning, the patient or QA phantom is setup to the laser isocenter, which is located outside of the magnetic bore with a 155 cm longitudinal shift to the treatment isocenter.

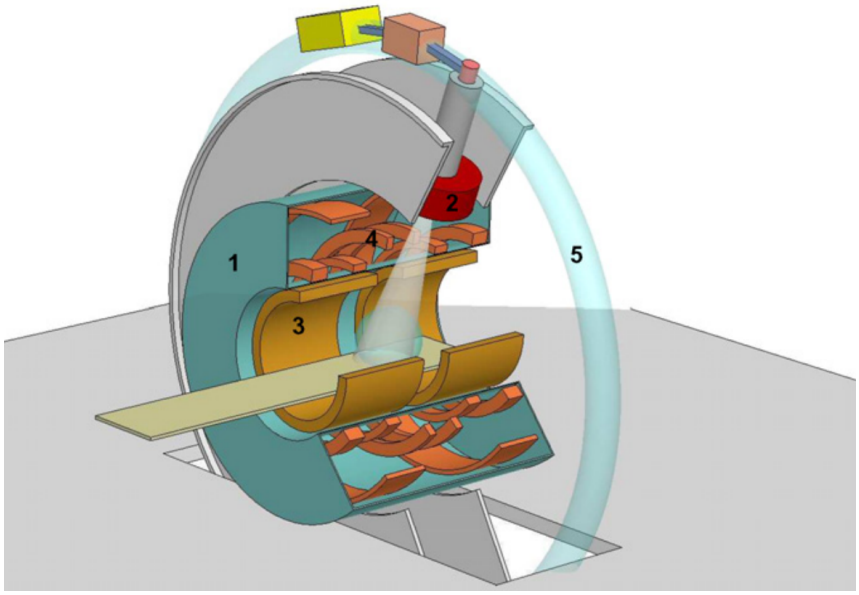

Figure 2.4: Sketch of the Elekta Unity concept. The blue is the 1.5 T MRI and the 7 MV accelerator is placed in a ring around it. The yellow is the split gradient coil and the superconducting coils are shown in orange. The light blue ring around the MRI indicates the low magnetic field toroid in the fringe field [38].

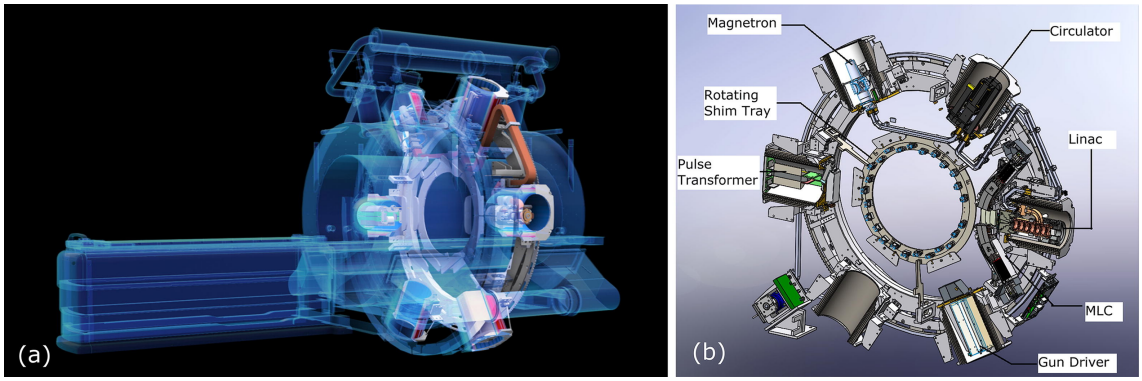

Figure 2.5: (a) Schematic drawing of the system depicting the main hardware components: superconducting double-donut magnet, circular radiation gantry and patient couch; (b) schematic drawing of the radiation gantry with linac components and MLC (Images courtesy of ViewRay Inc) [42].

2.2 Patient-specific quality assurance

As in the case of developed MR-linac systems, every radiation therapy (RT) unit and procedure must maintain the desired technical standard, regulated by quality assurance (QA) procedures. Quality assurance describes a quality policy, preparation, safety, and monitoring, as well as quality improvement, requiring each member of the radiation treatment team to work together on improving the devices and procedures.

Each step in radiation therapy may involve an individual quality assurance process, which requires an intensive resource. Therefore, it is essential to balance revised and unnecessary QA. Image registration, contouring, treatment planning, patient setup, and treatment delivery are the areas of radiotherapy for which QA is performed. To minimize accidents in oncology, organizations like the American Association of Physicists in Medicine (AAPM) publish guidelines for RT quality and safety that include prescriptive and risk analysis bases recommendations. Accordingly, each treatment's safety and accuracy for a patient must be checked. This process is known as patient-specific quality assurance (PSQA). For example, a PSQA verifies the dose calculated by the treatment planning system and treatment delivery precision, which is generally accomplished by comparing the calculated and measured dose distribution in a phantom [43].

2.2.1 Motivation - MR-linac patient QA

The instructions by the Swiss Society for Radiation Oncology (SRO), Swiss Society of Radiobiology and Medical Physics (SSRMP), and Swiss association of specialists in medical-technical radiology (SVMTRA) in "Recommendation for the preparation of a quality handbook for radiation oncology" to the radiation therapy community is guidance for dealing with the preparation of a quality handbook (This file is released by the Federal Office of Public Health (FOPH)). According to this handbook, [44], a patient-specific quality assurance focus areas should focus on imaging and target delineation, treatment planning, dosimetry, localization on treatment machine, treatment delivery, and overall patient management.

The MR-linac workflow contains a patient-specific QA process same as the conventional linac that evaluates optimized treatment plan irradiation in terms of dosimetry through phantom dose delivery and conventional dose measurement methods such as multipoint IC measurement, 2D film dosimetry, and quasi 3D diode arrays [45] [46]. Machine log files and either 2D fluence verification or 3D Monte Carlo-based dose reconstruction are other QA protocols mentioned in the literature [40]. Besides the verification of the patient's baseline treatment plan, due to the possibility of a daily treatment plan adaptation, while the patient is in the treatment position, online patient-specific QA is necessary before irradiation. However, for the online adaptation of the plans, an offline QA is performed after the irradiation is done, which is slower than the online QA [47].

There are several commercially available QA dosimeters and phantoms to perform accuracy verification of the complex treatment delivery techniques [48]. Nevertheless, almost all the conventional QA systems are not MR-compatible and cannot be used for dose measurements in the presence of the MR-linac's magnetic field. The currently available MR-compatible systems are described in the following section.

2.2.2 Existing MR-compatible patient QA systems

The ionizing radiation intensity is measured by a radiation detector translating radiation energy to an electrical signal by an electrometer. A specific detector calibration factor, like Gy/C, correlates the dose value with the detector signal, and depending on detector features and beam quality, other correction factors can be applied.

(a) Farmer ionization chamber

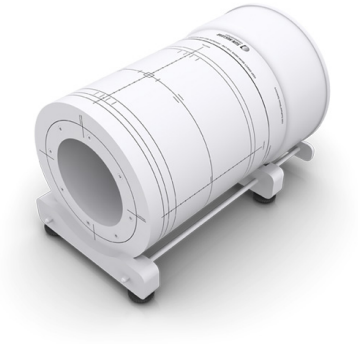

(b) ArcCHECK-MR phantom

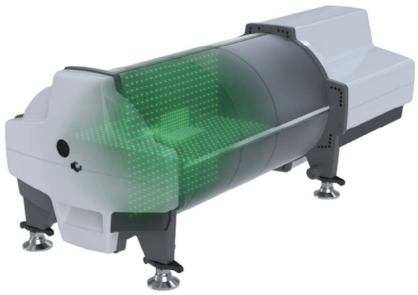

(c) Delta^4 + MR phantom

(d) OCTAVIUS 1500XDR detector

Figure 2.6: Patient-specific MR-compatible devices. (a) The Farmer ionization chamber (Type 30013) and the pmma build-up cap on the left (Image courtesy of PTW). (b) The ArcCHECK-MR phantom (Image courtesy of Sun Nuclear Corporation). (c) The Delta^4 + MR phantom with its plus-shaped detectors in green (Image courtesy of ScandiDos). (d) The OCTAVIUS 1500XDR detector (Image courtesy of PTW).

Diagnostic radiology, radiotherapy, and nuclear medicine use radiation detectors for dosimetry with three different detector types, the ionization chamber, the silicon diode detector, and the synthetic diamond diode detector based on three various measurement principles.

The MR-compatible commercially available QA systems at the moment of writing in figure 2.6 are the Farmer ionization chamber (Type TW30013, PTW, Freiburg, Germany), ArcCHECK-MR (Model 1220-MR, Sun Nuclear Corporation, Melbourne, USA), the Delta^4 + MR phantom (Scandidos AB, Uppsala, Sweden), and Octavius 1500 (PTW, Freiburg, Germany).

Fast sanity checks on the adapted plan [49], the geometric accuracy of the delivered dose using in-vivo EPID images [37], or the use of independent calculations performed by the linac log files [50] are additional methods established for the patient-specific QA [51].

Farmer ionization chamber

The ionization chamber (IC) is a detector consisting of two electrodes with a voltage between 100 and 1000 V and a 0.005 to 50000 cm^3 gas volume in between where the ionizing radiation directly creates ion pairs. The electrodes attract the charged particles, generating a 10^{-14} to 10^{-7} A current, which is measured by the electrometer.

The standard ionization chamber for RT absolute dose measurements is the Farmer ionization chamber (Type TW30013), which is waterproofed, MR safe, and can be used

in water or solid state phantoms. Figure 2.6a shows the chamber with its polymethylmethacrylate (PMMA) build-up cap on the left. The dosimetry protocols published the required correction factors to determine the absorbed dose to water or air kerma [52].

The kinetic energy released per unit mass (KERMA) is a radiation quantity measuring the absorbed radiation energy in a unit mass of air. It has a unit of J/Kg, which is also called Gray (Gy) as a radiation unit.

ArcCHECK-MR phantom

The ArcCHECK-MR (Sun Nuclear Corporation, Melbourne, USA) is a cylindrical water-equivalent PMMA phantom presented in figure 2.6b with 1386 SunPoint diode detectors arranged in a 10 mm diode spacing spiral pattern. The complete compatibility with current MR-linac systems is adapted by extending the power supply to the 5.0 gauss line. The phantom also features an interior cavity, which enables a wide variety of detectors and tissue equivalent inserts to be mounted. In addition, a comparison between the delivered and planned dose is possible by ArcCHECK software [40] [45].

Delta^4 + MR phantom

The research and development department of Scandidos AB (Uppsala, Sweden) and the de Vries group (Department of Radiation Oncology, University Medical Center Utrecht, Utrecht, Netherlands) have developed the Delta^4+MR phantom from the Delta^{4}Phantom+ (Scandidos AB, Uppsala, Sweden). The technical features of this phantom are the same as the Delta^4 phantom, and it is adapted to be fully compatible with existing MR-linac systems. Figure 2.6c represents the inside of the Delta^4 phantom, showing its plus-shaped detector arrays in green.

Delta^4 + MR phantom is a cylindrical shaped PMMA phantom and contains two orthogonal detector boards parallel to the coronal and sagittal plane, in a total of 1069 p-type Si-diodes detectors that are placed in the target region. The silicon semiconductors have an n-type layer of silicon interacting with a p-type silicon layer, creating an isolating internal zone by causing electrons to move from the n region to the p detector layer. The incident radiation hits the sensitive layer of the detector in the intrinsic zone and frees electrons. These electrons move to the positively charged p region, generating a current.

The electronics are separated and placed on a trolley with the phantom, which makes their set-up fast. It is the only system that measures the dose distribution in the isocenter region, and its software allows the user to instantly analyze the plan by comparing the delivered dose with the dose predicted by the Viewray treatment planning system [53].

OCTAVIUS 1500XDR detector

The OCTAVIUS 1500XDR detector in figure 2.6d is an MR-compatible 2-D array detector with 1405 built-in cubic ionization chambers uniformly arranged on a 27 x 27 cm^2 matrix. It is suitable for patient plan verification and also machine QA with a 7.1 mm center-to-center diagonal detector spacing [51].

Chapter 3

Evaluation of the Delta^4 + MR phantom

The purpose of this work was to examine the Delta^4 + MR phantom extensively in 0.345 T magnetic field and give a general report on the early clinical experience of using the phantom for patient-specific QA.

3.1 Material and Methods

The daily output stability, dose linearity, field size dependency, angular dependency, and planned versus delivered dose comparison tests were performed on the Delta^4 + MR phantom on the 0.345 T superconducting MRIdian MR-linac. The Delta^4 + MR phantom was placed at the isocenter for all the measurements and the data evaluation was performed with R language on RStudio software [54]. Figure 3.1 represents the setup of the phantom for each test.

3.1.1 Daily output stability of the MR-linac

The daily output of the machine was measured within fourteen months, from February 2019 until April 2020, with the Delta^4 + MR phantom to daily check the performance stability of the phantom on the machine. Each day the phantom was irradiated by a $9.96 \times 9.96\,\text{cm}^2$ open field size beam with 143.8 monitor units at 315°gantry angle. Monitor unit (MU) measures the generated radiation "beam-on" time produced by the linac. One MU is equal to 1 cGy of absorbed dose in water [55]. The intention of choosing this particular gantry angle was equally irradiating both plus-shaped detector arrays of the Delta^4 + MR phantom. Figure 3.1a shows the setup of the phantom for the measurements.

The daily output of the phantom was evaluated by the relative response (R) suggested by Bedford [56] with equation 3.1.1 for a fixed planned dose distribution. The suggested daily correction factor (SDCF) measures the overall response of the phantom to a simple open field by providing a correction factor to achieve the required planned dose distribution.

$$R = \frac{1}{\text{SDCF}} \tag{3.1.1}$$

The Scandidose Delta^4 software (version 1.00.0180) measures the SDCF via the 3.1.2 equation, where N is the number of central detectors in the phantom, i is these detectors index, D^i_{TPS} is the planned dose distribution obtained from the treatment planning system (TPS) at the location corresponding to detector i, and D^i_{D4} is the phantom's measured

dose at detector i. The SDCF was measured three times with the Scandidose Delta^4 software and the average value over these measurements was recorded in a file.

$$\text{SDCF} = \sum_{i=1}^{N} D^i_{\text{TPS}} / \sum_{i=1}^{N} D^i_{D4} \tag{3.1.2}$$

After taking the temperature and pressure of the treatment room, the daily output was measured independently with the Farmer ionization chamber (PTW Freiburg, Type TW30013). The chamber was placed inside a solid water block and irradiated with a $9.96 \times 9.96\,\text{cm}^2$ open field beam with 100 MU at the gantry angle of 0°.

The Farmer chamber is designed for beam irradiation from the top with standard 100 MU measurement and not the random 143 MU like the Delta^4 + MR phantom. However, since all the measurements are relative to the reference machine's calibration measurements, the difference between the two setups is not an issue. Furthermore, the beam angle was not 315°like the Delta^4 + MR phantom as it would irradiate the block from a less reproducible tilted edge. The chamber's output was compared to the output of the Delta^4 + MR phantom to check the phantom's stability over time. The relative differences between the measured outputs were calculated and normalized using the *scale* function in R.

3.1.2 Dose linearity

The linearity of the dose response measured with the Delta^4 + MR phantom was evaluated using the same radiation setup for the daily output stability test, a 143.8 MU $9.96 \times 9.96\text{cm}^2$ open field beam with the gantry angle 315°. Doses with 0.2 intervals from 0.2 to 1.2 Gy were irradiated on the phantom, and their absolute measured dose was recorded. Since it is not possible to set a specific number of MUs for plans on the TPS, they were designed based on different dose values. The delivered MUs and their corresponding planned dose are 28 (0.2 Gy), 56 (0.4 Gy), 84 (0.6 Gy), 112 (0.8 Gy), 140 (1.0 Gy), and 168 (1.2 Gy) MU. The correlation between the delivered MU and the measured dose was calculated with the *cor* R function [54].

3.1.3 Field size dependency

The field size dependency of the measured dose with respect to the planned dose distribution was analyzed for different beams with square field sizes of $1.66 \times 1.66\,\text{cm}^2$, $4.16 \times 4.15\,\text{cm}^2$, $9.96 \times 9.96\,\text{cm}^2$, $14.94 \times 14.94\,\text{cm}^2$, and $19.92 \times 19.92\,\text{cm}^2$ at gantry angle 315°. Figure 3.1b demonstrates an example setup for these measurements. The Delta^4 phantom software measured the delivered dose, SDCF, median deviation, and gamma agreement index (GAI) with two different evaluation criteria, 3%/3mm and 2%/2mm, for each field size. The plans were delivered three times for each field size and evaluated by their average. The gamma index (γ) evaluation is a dimensionless metric measuring dose difference (DD) and distance to agreement (DTA) criteria. It evaluates the measured dose distributions in detector systems against the distribution predicted by TPS [57]. The points passing the DD/DTA criteria have a γ agreement index smaller than one. The total percentage of detectors achieving γ less than one for the given DD/DTA criteria is measured, and the QA pass or fail threshold is set [58][59][48].

3.1.4 Angular dependency of the Delta^4 + MR phantom

To determine the angular dependency of the detectors, the same $9.96 \times 9.96\,\text{cm}^2$ field was irradiated three times onto the Delta^4+MR phantom from equally distributed angles every 22°with the setup presented in figure 3.1c. The reason for choosing this specific interval

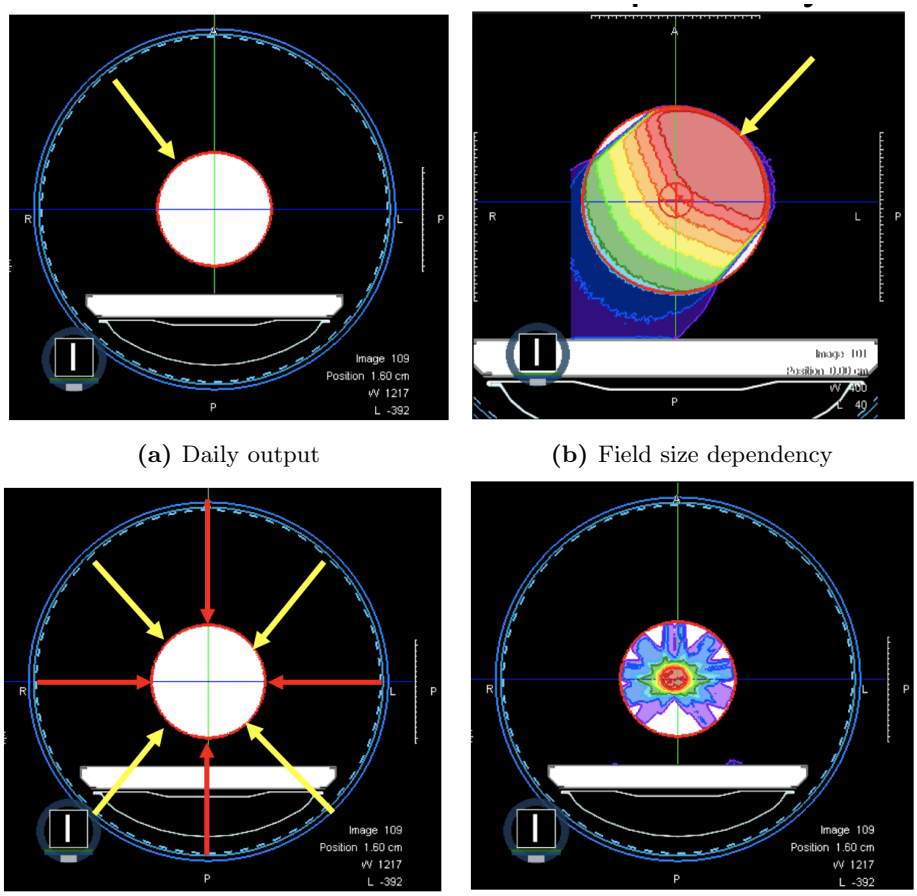

(a) Daily output **(b)** Field size dependency

(c) Angular dependency **(d)** Patient QA

Figure 3.1: The QA measurement setups. (a) Phantom's daily output on the MRIdian. (b) Field size dependency of the phantom. (c) Angular dependency of the phantom. (d) Sample patient QA for each treatment plan.

was to evaluate the 0°, 90°, 180°, and 270°gantry angles as they are parallel to the detector plates and most probable to show beam angular differences. The GAI calculated in the Delta^4 software was used for the evaluation and compared to the planned dose distribution.

3.1.5 Patient-specific QA

In total, 205 treatment plans (41 prostate, 40 lung, 26 liver and 8 head and neck) from real patients were calculated on a virtually designed Delta^4 + MR phantom in the ViewRay treatment planning system with the Monte Carlo algorithm, and assessed by the Delta^4 + MR phantom. The composite dose of all beams per patient plan was verified, and Scandidos provided the electron density map for the designed virtual Delta^4 + MR phantom. A global GAI of more than 95% was considered as a successful QA using 3% global dose difference, a DTA of 3 mm, and a dose threshold of 20% of the maximum dose. An additional evaluation was done with 2 mm and 2% GAI criteria. Figure 3.1d shows an example color map of the delivered plan on the Delta^4+MR phantom for a patient-specific QA.

3.2 Results

After delivering all the plans on the Delta^4 + MR phantom and recording the results from the Delta^4 software manually, they were sorted and analyzed in R.

3.2.1 Daily output stability of the MR-linac

The Delta^4 + MR phantom and the Farmer chamber daily output deviation were both within the 2.00% clinically accepted range. The maximum output deviation was 1.92% for the Delta^4 + MR phantom and 1.00% for the Farmer Chamber. All values are shown in figure 3.2.

3.2.2 Dose linearity

As can be seen in figure 3.3, the absolute measured dose increases linearly with the planned dose. Using Pearson's product-moment correlation test, there was a 0.99 correlation between the planned MU and the delivered dose with standard deviation of 0.35 Gy/MU.

3.2.3 Field size dependency

The deviation between the measured and the calculated output is smaller than 2.00%. The largest deviation is 1.46% for the $1.66 \times 1.66\,\mathrm{cm}^2$ field. From the smallest field size to the 2nd smallest field size the deviation is decreasing. The average gamma agreement for 2%/2 mm criteria was $97.07 \pm 3.14\%$ and for the 3%/3 mm was $99.97 \pm 0.06\%$. All data are represented in figure 3.4.

3.2.4 Angular dependency of the Delta^4 + MR phantom

The average gamma passing rates for the angular dependency of the phantom was $99.3 \pm 1.4\%$ for 3%/3 mm and $95.2 \pm 4.8\%$ for 2%/2 mm criteria including the 0°, 90°, 180°, and 270°gantry angles. Excluding these four angles, the gamma agreement increased to $99.7 \pm 0.4\%$ for 3%/3 mm criteria and $96.6 \pm 3.4\%$ for 2%/2 mm. The measured values are shown in figure 3.5.

3.2.5 Patient-specific QA

Out of the first 205 measured patient plans, only one plan failed the gamma passing criteria of $> 95\%$ (3%/3 mm), the average gamma passing rate was $99.8 \pm 0.5\%$ for 3%/3 mm and $98.6 \pm 2.4\%$ for 2%/2 mm criteria. The 26 delivered liver plans had the best evaluation with 100% gamma passing rate for 3%/3mm and 99.6% for 2%/2mm criteria. For the 8 head and neck measured plans, the average gamma passing rate was $99.9 \pm 0.1\%$ for 3%/3 mm and $98.6 \pm 1.2\%$ for 2%/2 mm criteria. Figure 3.6 shows the histogram for all the delivered and the head and neck plans and table 3.1 presents the average gamma passing rates for 3%/3 mm and 2%/2 mm criteria for each site and the total delivered plans.

Site	Number of plans	3%/3 GAI	2%/2 GAI
Prostate	41	$99.6 \pm 0.8\%$	$99.5 \pm 3.1\%$
Lung	40	$99.7 \pm 0.2\%$	$99.3 \pm 1.9\%$
Liver	26	$100 \pm 0.0\%$	$99.6 \pm 0.8\%$
Head and Neck	8	$99.9 \pm 0.1\%$	$98.6 \pm 1.2\%$
Total	205	$99.8 \pm 0.5\%$	$98.6 \pm 2.4\%$

Table 3.1: Measured GAI values with different criteria and the number of delivered plans for each treatment site.

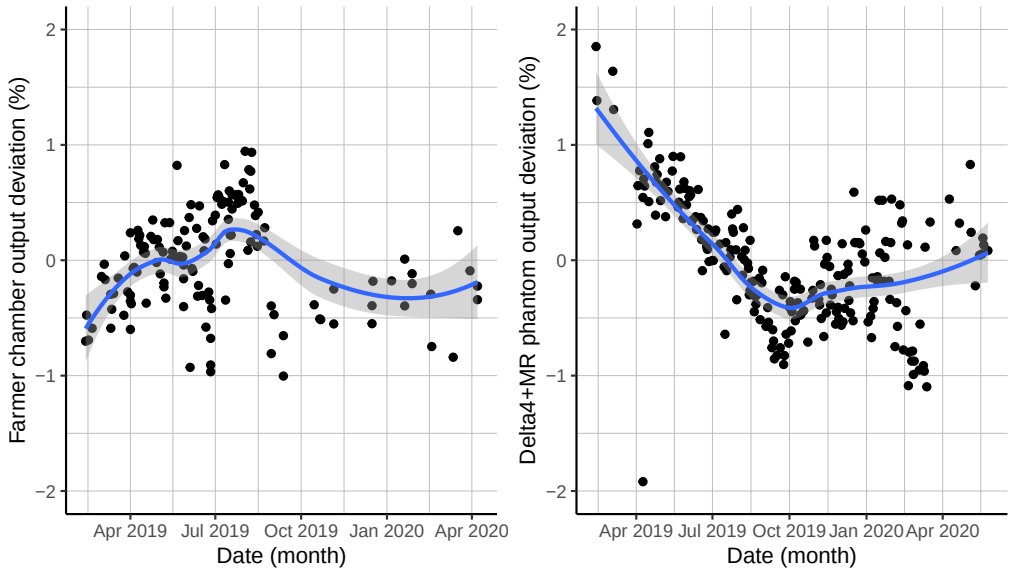

Figure 3.2: The daily output variation of the MRIdian values measured with the Delta^4 + MR phantom and Farmer ionization chamber, normalized by the *scale* function and fitted with *geom_smooth* from the *ggplot2* package in R [54].

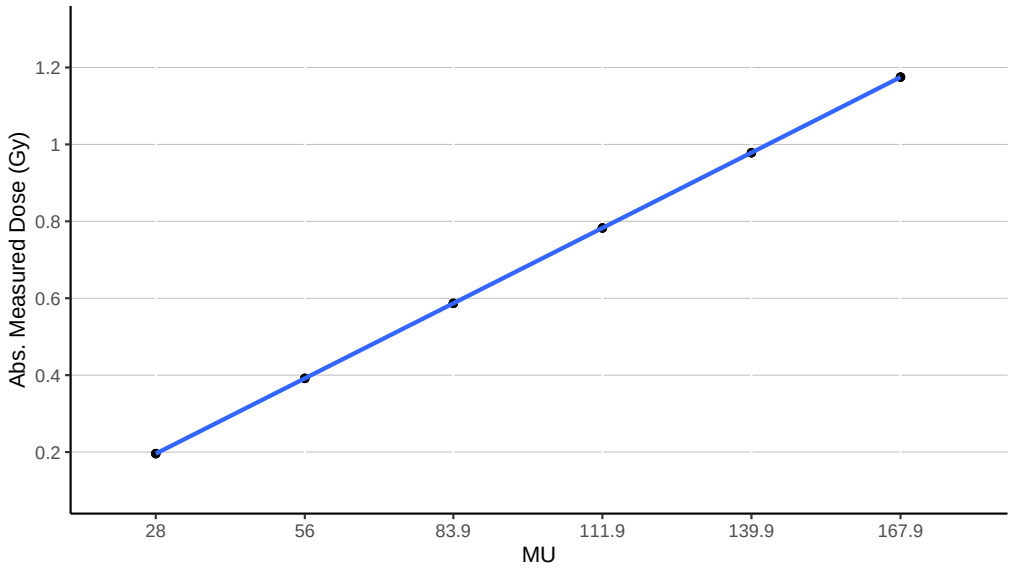

Figure 3.3: The dose linearity of the Delta^4 + MR phantom, absolute delivered dose as a function of planned monitor units, Standard deviation = 0.34 Gy/MU

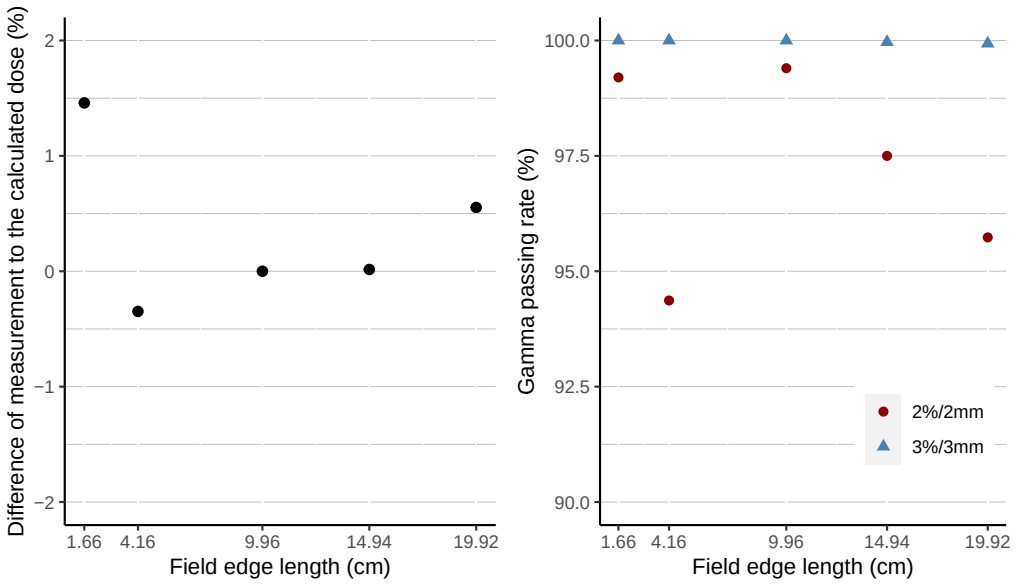

Figure 3.4: The field size dependency of Delta^4 + MR phantom, left: The response factor, R, has been taken as an output and they are normalized to the 10x10 cm^2 field's output, right: GAI with 2%/2 mm and 3%/3 mm criteria for different square field sizes.

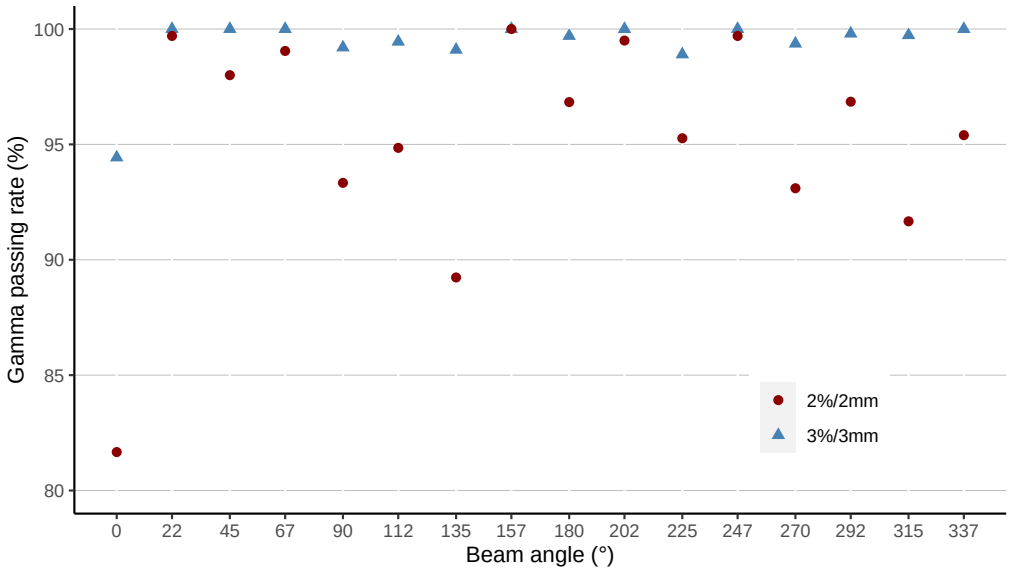

Figure 3.5: The angular dependency of the Delta^4 + MR phantom is evaluated by measuring different gamma passing rate criteria for different gantry angles.

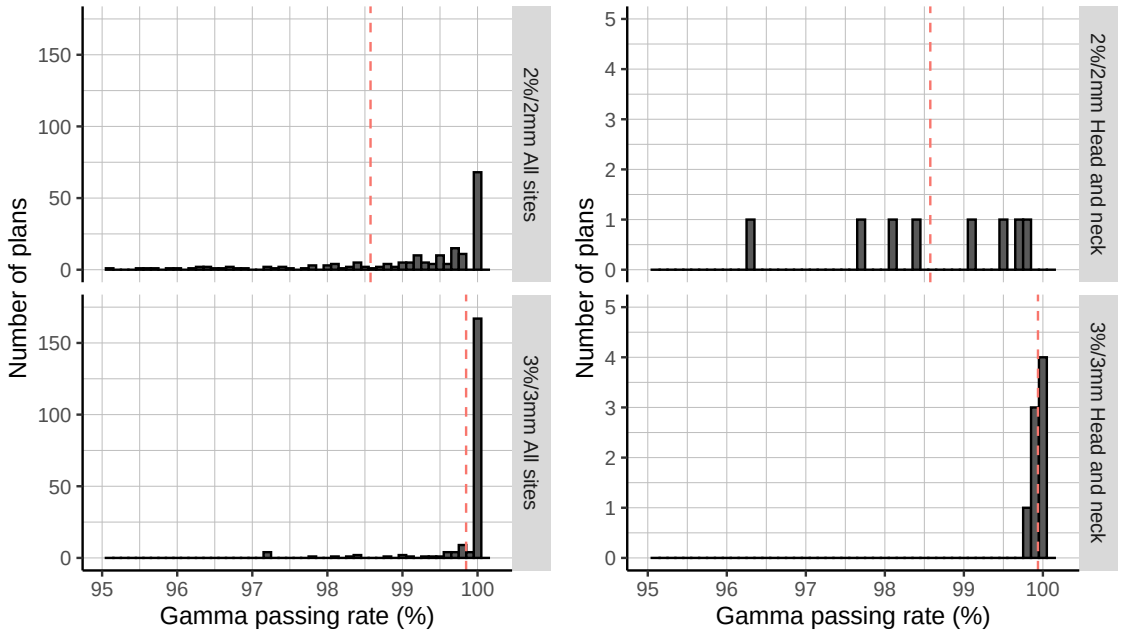

Figure 3.6: Histogram for gamma passing rates with 3%/3 mm and 2%/2 mm criteria with the overall average passing rate for each group above 98% (red dashed lines), left: the total delivered plans with different sites (total of 204 plans), right: delivered head and neck patient plans (total of 8 plans)

Chapter 4

Modulation complexity score

The IMRT technique delivers a tumor's therapeutic dose and optimizes the sparing of OAR by multiplying different beam fluences from different static gantry angles. The jaws and MLC shape irregular beam openings to create different beam fluences. However, since MRIdian has no jaws, the fluences are only generated by the MLC. Each angle has its own required modulated fluence created by multiple different beam opening (segment) sum.

The modulation complexity score (MCS) is a metric for assessing the complexity and deliverability of patient-specific treatment plans and is calculated based on the TPS information, like the position of the leaves and the number of monitor units of each segment. A treatment plan with zero complexity, like an open rectangular field, has an MCS of 1.0 and its score decreases as the segments become more irregular. The MCS is based on the leaf sequence variability (LSV) and the aperture area variability (AAV) quantifying the intra- and inter-segment shape variability for each beam and plan, explained in the next section [60]. This metric provides more information about the delivery of the dose than a simple beam parameter, like the number of segments or MU, which can be useful in the treatment planning and the QA process of the MR-linac.

4.1 Metrics calculation and analysis

The MCS adapted from the work by McNiven [60] and other introduced metrics assess the plan complexity for the MR-linac treatment plans. After defining and adjusting the metrics for the MR-linac, they were implemented and evaluated in MATLAB [61] using the DICOM file of every treatment plan. Each treatment plan has several beams made up of several segments formed by the MLC.

4.1.1 MCS calculation

The segment shape, area, and weight, calculated based on the data from the TPS, determines the MCS for each beam. The LSV parameter determines the segment shape variability in each plan, taking into consideration the change in the leaf position from adjacent MLC leaves, as defined in the equation 4.1.1 below, which is the variability in the left MLC bank times the variability in the right MLC bank.

$$\mathrm{LSV} = \frac{\sum_{n=1}^{N} (\mathrm{LMD} - (\mathrm{L}_n - \mathrm{L}_{n+1}))}{N \times \mathrm{LMD}} \times \frac{\sum_{n=1}^{N} (\mathrm{RMD} - (\mathrm{R}_n - \mathrm{R}_{n+1}))}{N \times \mathrm{RMD}} \tag{4.1.1}$$

In this equation, the position of each leaf is L for the left bank and R for the right one, N is the number of open leaves in each segment, and n is the leaf index. The LMD and RMD are the maximum difference in leaf positions for the left and right bank as defined in equations 4.1.2 and 4.1.3.

$$\mathrm{LMD} = \max_n(\mathrm{L}_n) - \min_n(\mathrm{L}_n) \tag{4.1.2}$$

$$\mathrm{RMD} = \max_n(\mathrm{R}_n) - \min_n(\mathrm{R}_n) \tag{4.1.3}$$

The AAV characterizes the variation in segment area relative to the maximum aperture defined by all of the segments using the leaf position information as presented in equation 4.1.4, where segments with a similar area to the maximum aperture in each beam contribute to a larger score. The maximum leaf position throughout the whole beam is LM for the left MLC bank and RM for the right one.

$$\mathrm{AAV} = \sum_{n=1}^{N}(L_n - R_n) \times \frac{1}{N \times (LM - RM)} \tag{4.1.4}$$

Equation 4.1.5 determines the final beam MCS, $MCSB$, which incorporates the relative segment weight, AAV, and LSV of each segment. The relative segment weight is the number of MUs per segment, $MUSG$, divided by the total number of MUs per beam, MUB, and I is the number of segments in the beam.

$$\mathrm{MCSB} = \sum_{i=1}^{I}\left[\mathrm{AAV}_i \times \mathrm{LSV}_i \times \frac{\mathrm{MUSG}_i}{\mathrm{MUB}}\right] \tag{4.1.5}$$

The total plan complexity, MCS, is defined by another metric in equation 4.1.6 that is the beam MCS weighted by the relative MU of each beam, MUB, in the plan. In this equation J is the number of beams in the total plan and the total number of MUs in the plan is MUP [60].

$$\mathrm{MCS} = \sum_{j=1}^{J}\left[\mathrm{MCSB}_j \times \frac{\mathrm{MUB}_j}{\mathrm{MUP}}\right] \tag{4.1.6}$$

4.1.2 SMUS and SFS calculation

The small monitor unit score (SMUS) assesses the performance of plans with small MU per beam on the MRIdian considering it might be difficult for the MR-linac to deliver a small amount of dose.

The SMUS ranges from 0 for all segments with lower number of MUs lower than the criteria x to 1 indicating the number of MUs for all segments is higher than x. Equation 4.1.7 defines the SMUS metric, where x is the desired MU limit, N is the total number of segments in the beam, and n is the segment index.

$$\mathrm{SMUS_x} = \frac{\mathrm{MUP} - \sum_{n=1}^{N}\mathrm{MU}_n * \mathrm{I}_n}{\mathrm{MUP}} \tag{4.1.7}$$

where I_n is defined as:

$$\mathrm{I}_n = \begin{cases} 1 & \text{for } \mathrm{MU}_n < \mathrm{x} \\ 0 & \text{otherwise} \end{cases} \tag{4.1.8}$$

The small field score (SFS) evaluates the plan's performance delivered by small beam openings. The small segments might have an impact on plan performance since the dosimetry of small fields is challenging. The SFS ranges from 0 for a beam with no segment area smaller to 1 for all segments larger than the criteria. Equation 4.1.9 defines the SFS metric, where x is the surface area threshold, N is the total number of segments in the beam, and n is the segment index. The weighting factor is the number of MUs per segment.

$$\mathrm{SFS_x} = \frac{\mathrm{MUP} - \sum_{n=1}^{N} \mathrm{MU}_n * \mathrm{J}_n}{\mathrm{MUP}} \tag{4.1.9}$$

where J_n is defined as:

$$\mathrm{J}_n = \begin{cases} 1 & \text{if area of segment n} < \mathrm{x} \\ 0 & \text{otherwise} \end{cases} \tag{4.1.10}$$

4.1.3 Metrics implementation and evaluation

The MCS, SFS, and SMUS evaluated multiple chosen treatment sites with different complexity ranges, such as lung, prostate, and head and neck. In total, 278 treatment plans, which have passed the patient QA and been delivered to the patient by the MRIdian MR-linac, were exported from the TPS for metrics evaluation. DICOM files store the characteristics of the plans that were read by the *dicominfo* MATLAB function.

Furthermore, 13 head and neck, 32 liver, 47 lung, and 56 prostate plans were selected for further evaluation because of their special characteristics. Table 4.1 shows an overall summary of specific features for each treatment site.

The *adaptMLC* function written in MATLAB sorts the leaves positions by putting them into two left and right groups and stores their coordinates in two arrays. The *MCScalcProg* program calculates the MCS for each plan with the *posmax* and *LSVsegment* function written in MATLAB with the equations introduced in section 4.1.1.

The *SFSxCalc* and *MUSxCalc* functions measure SFS and SMUS metrics for each plan with five different criteria. The criteria are 5, 10, 20, 50, and 100 and they are in mm^2 for the SFS and number of MU for the SMUS. Both functions are implemented in MATLAB.

Finally, an automated version of the programs simultaneously calculated metrics for all the chosen treatment plans and saved the results for further metric evaluations. For more details about the program and functions, one can refer to the appendix A.

The head and neck, liver, lung, and prostate sites were selected for the metric evaluations with a total of 153, of which 112 were SBRT and 41 were IMRT delivered treatment plans. All the head and neck plans are IMRT, and the lungs are SBRT plans. The liver has 23 SBRT and 10 IMRT plans, and the prostate site has 42 SBRT and 18 IMRT plans. The main difference between IMRT and SBRT technique is the prescribed dose per fraction, which is 2-3 Gy per fraction for the IMRT and 5-10 Gy per fraction for the SBRT plans.

The correlation coefficients between the MCS and plan's total number of segments, the total number of MUs, and the total number of MUs over the total number of segments ratio were calculated. The MCS values were plotted versus these features with a linear regression model with equation 4.1.11, where x can be the plan's total number of segments, the total number of MUs, or the total number of MUs over the total number of segments ratio. Finally, the GAI correlation coefficients with the MCS and the total number of MUs were calculated to determine the impact of the introduced metrics on the GAI values.

$$\mathrm{MCS_{treatment\ plan}} = \mathrm{p_1 x} + \mathrm{p_2} \tag{4.1.11}$$

From the SMUS and SFS metrics boxplots, the criteria x where the data begin to spread were chosen for further metrics evaluation. The SMUS and SFS correlation coefficients with the plan's total number of segments, the total number of MUs, the total number of MUs over the total number of segments ratio, and MCS were calculated. At last, the GAI correlation coefficients with the SMUS and SFS were calculated to determine the impact of these introduced metrics on the GAI values.

The correlation coefficients were determined by the *corrcoef* MATLAB function using the Pearson method defined in equation 4.1.12., where the μ and σ are the mean and standard deviation, respectively. Also, all the calculations and plots are performed in MATLAB.

$$\rho(A,B) = \frac{1}{N-1}\sum_{i=1}^{N}\left(\overline{\frac{A_i-\mu_A}{\sigma_A}}\right)\left(\overline{\frac{B_i-\mu_B}{\sigma_B}}\right) \tag{4.1.12}$$

Site	#plans	#beams	#segments	#MUs	MCS
Head and Neck	13	10 (9-11)	87 (70-120)	922 (629-1451)	0.242 (0.118-0.351)
Liver	33	10 (9-11)	53 (39-70)	1577 (619-3745)	0.402 (0.165-0.635)
Lung	47	11 (9-12)	25 (15-55)	3131 (700-4549)	0.386 (0.109-0.751)
Prostate	60	10 (8-11)	55 (20-72)	1808 (536-3934)	0.435 (0.161-0.664)
Total	278	10 (6-12)	51 (11-120)	2134 (284-9809)	0.384 (0.085-0.752)

Table 4.1: Characteristic summary of evaluated treatment plans. The table shows the total number of plans, beams, segments, MUs, and MCS for each treatment site. Numbers present the average and their range in parenthesis for each feature.

4.2 Results

The correlation coefficients higher than 0.3 are considered significant and highlighted with asterisks in the tables.

4.2.1 MCS evaluation

Table 4.1 shows the average MCS and its range in parenthesis for each treatment site and the total delivered plans. The average MCS value is 0.38 for 278 delivered plans with a range of 0.08 to 0.75. The head and neck plans have the lowest average value of 0.24 and a range of 0.12 to 0.35. widest The lung plans have the broadest range of MCS from 0.11 to 0.75.

Figures 4.1 and 4.2 present the MCS histogram of delivered plans for all and per each treatment site.

4.2.2 MCS correlation with other features of the plan

The MCS correlation coefficient with the plan's total number of segments is -0.09, with the plan's total number of MUs is -0.01, and 0.06 with the plan's total number of MUs over the total number of segments ratio. The IMRT plans have higher correlation coefficients with -0.68 for the total number of segments and -0.65 for the total number of MUs. Table 4.2 shows these correlation coefficients and their p-value in parenthesis for all the delivered plans and the two different planning methods, SBRT and IMRT.

The calculated correlation coefficients for each treatment site are presented in table 4.3. The head and neck has the highest correlation coefficients with -0.71 for the total number of segments, -0.87 for the total number of MUs, and -0.68 for the ratio. The total liver and prostate plans have the lowest correlations. Their calculated coefficients based on the planning method are presented in tables 4.4 and 4.5.

The MCS values versus plans features plots for each treatment site are presented in appendix B.

4.2.3 MCS and total number of MUs vs. gamma agreement index

There was no correlation between GAI, with 3%/3mm and 2%/2mm criteria, MCS, and the total number of MUs for the delivered plans. However, there was a correlation between GAI and the total number of MUs for the lung and head and neck site, and between GAI with 2%/2mm criteria and MCS for the head and neck plans.

Table 4.6 represents the correlation coefficients for all the delivered plans and per each treatment site. The relations between GAI, MCS, and the total number of MUs for all the delivered plans and each treatment site are presented in appendix B.

Total plans correlations	All	SBRT	IMRT
Number of segments vs. MCS	-0.09 (0.34)	0.09 (0.40)	-0.68 (0.00)*
Number of MU vs. MCS	-0.01 (0.95)	-0.04 (0.72)	-0.65 (0.00)*
Number of MU/seg vs. MCS	0.06 (0.51)	0.07 (0.50)	0.30 (0.07)*

Table 4.2: MCS correlation coefficients with the total number of segments, MUs, and MUs over the total number of segments for each treatment plan for all the 153 delivered plans, of which 112 were SBRT and 41 were IMRT plans. The values in parenthesis are the corresponding p-values for each coefficient.

Correlations	#MU	#Segments	#MU/#Segments
Head and Neck	-0.71 (0.01)*	-0.87 (0.00)*	-0.68 (0.00)*
Liver	0.45 (0.01)*	-0.28 (0.12)*	-0.39 (0.03)*
Lung	-0.34 (0.02)*	0.06 (0.68)	0.29 (0.05)*
Prostate	0.22 (0.11)	0.07 (0.59)	-0.05 (0.70)

Table 4.3: MCS correlation coefficients with the total number of segments, MUs, and MUs over the total number of segments for each treatment plan for each treatment site. The values in parenthesis are the corresponding p-values for each coefficient.

Liver plans correlations	All	SBRT	IMRT
Number of segments vs. MCS	0.45 (0.01)*	0.40 (0.08)*	0.53 (0.22)*
Number of MU vs. MCS	-0.28 (0.12)*	-0.15 (0.51)	-0.64 (0.12)*
Number of MU/seg vs. MCS	-0.39 (0.03)*	-0.27 (0.25)*	-0.53 (0.22)*

Table 4.4: MCS correlation coefficients with the total number of segments, MUs, and MUs over the total number of segments for each treatment plan for all the 33 liver plans, of which 23 were SBRT and 10 were IMRT. The values in parenthesis are the corresponding p-values for each coefficient.

Prostate plans correlations	All	SBRT	IMRT
Number of segments vs. MCS	0.22 (0.11)	0.03 (0.88)	-0.03 (0.92)
Number of MU vs. MCS	0.07 (0.59)	-0.32 (0.06)*	-0.25 (0.37)
Number of MU/seg vs. MCS	-0.05 (0.70)	-0.13 (0.44)	-0.12 (0.66)

Table 4.5: MCS correlation coefficients with the total number of segments, MUs, and MUs over the total number of segments for each treatment plan for all the 60 protate plans, of which 42 were SBRT and 18 were IMRT. The values in parenthesis are the corresponding p-values for each coefficient.

Correlations	3%/3mm vs. MCS	2%/2mm vs. MCS	3%/3mm vs. #MU	2%/2mm vs. #MU
Head and Neck	0.20 (0.52)	0.34 (0.26)*	-0.33 (0.28)*	-0.53 (0.06)*
Liver	0.20 (0.27)	0.20 (0.27)	0.12 (0.52)	0.12 (0.51)
Lung	0.02 (0.88)	0.03 (0.83)	0.35 (0.01)*	0.35 (0.02)*
Prostate	0.04 (0.77)	-0.05 (0.70)	-0.05 (0.74)	-0.14 (0.30)
Total	-0.12 (0.21)	-0.09 (0.36)	0.13 (0.19)	0.12 (0.20)

Table 4.6: GAI correlation coefficients with the MCS and total number of MUs for all the delivered plans. The values in parenthesis are the corresponding p-values for each coefficient.

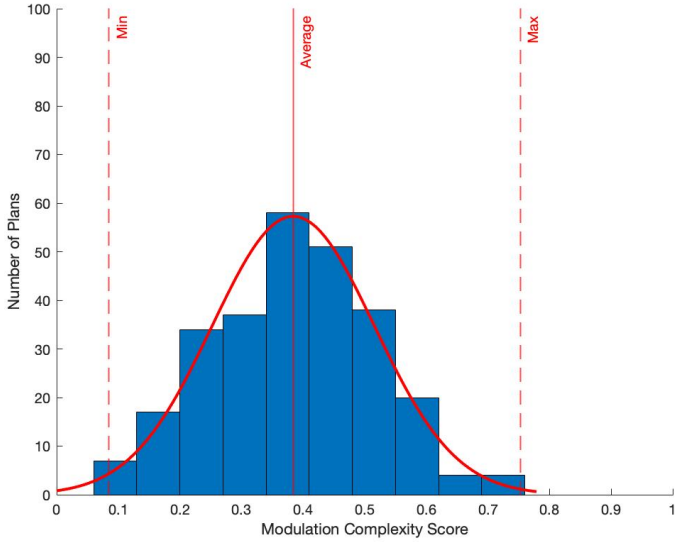

Figure 4.1: The MCS histogram for all the delivered plans. Solid red line is the mean value of 0.4 and the red dashed lines are the minimum and maximum MCS values.

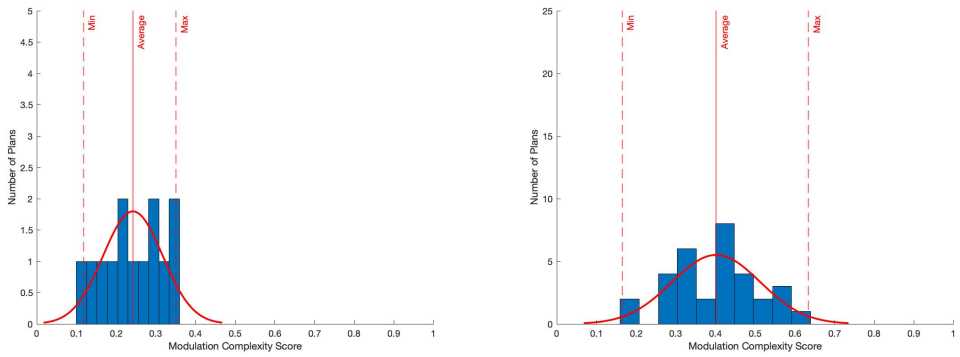

(a) Head and Neck

(b) Liver

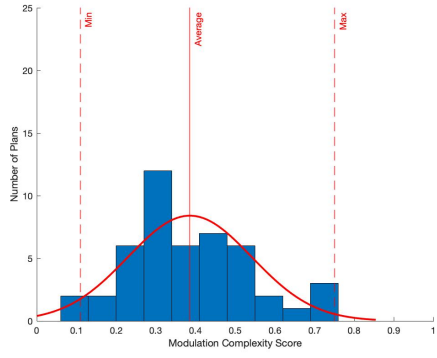

(c) Lung

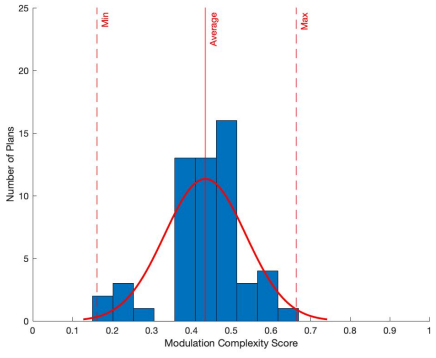

(d) Prostate

Figure 4.2: The MCS histogram for each treatment site. Solid red line is the average and the red dashed lines are the minimum and maximum MCS values. Lung has the widest and head and neck has the narrowest range of MCS values.

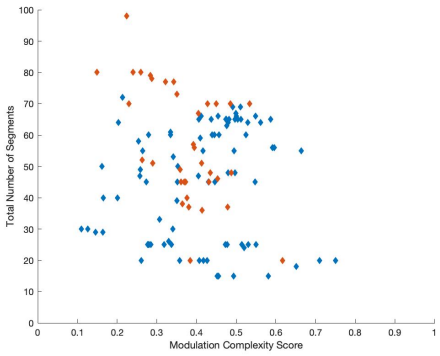

(a) Number of segments vs. MCS

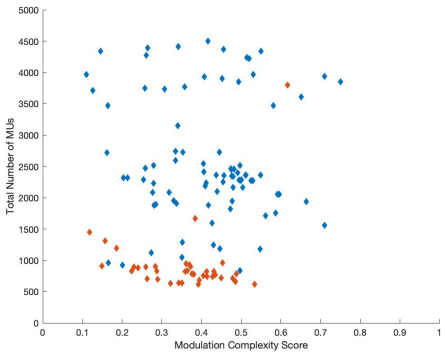

(b) Number of MUs vs. MCS

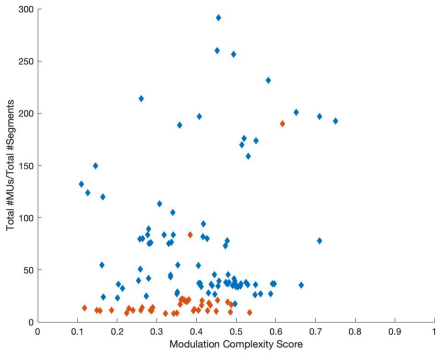

(c) Number of MU/segments vs. MCS

Figure 4.3: MCS relation with the total number of segments, MUs, and MUs over the total number of segments for all the delivered plans. Red dots are the IMRT, and blue ones are SBRT plans.

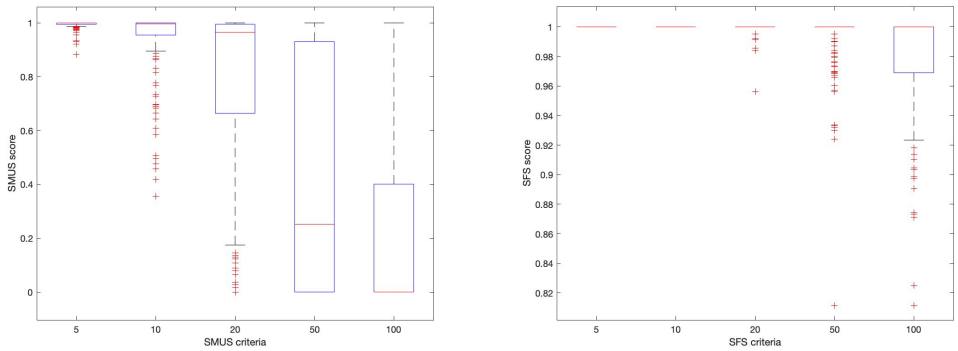

(a) SMUS values **(b)** SFS values

Figure 4.4: SMUS and SFS boxplots for all the delivered plans with criteria 5, 10, 20, 50, and 100. The x-axis for SMUS metric is the threshold criteria of total number of MUs per segment, and for SFS is the threshold criteria of segment area in mm^2.

Correlations	#MU	#Segments	#MU/#Segments	MCS
SMUS 10	0.52 (0.00)*	-0.56 (0.00)*	0.38 (0.00)*	0.17 (0.07)
SMUS 20	0.69 (0.00)*	-0.57 (0.00)*	0.52 (0.00)*	0.18 (0.06)
SFS 50	-0.18 (0.07)	-0.01 (0.95)	-0.07 (0.46)	0.29 (0.00)*
SFS 100	-0.28 (0.00)*	0.08 (0.43)	-0.21 (0.03)	0.38 (0.00)*

Table 4.7: SMUS and SFS correlation with other features of the plan. The 10 and 20 for the SMUS metric and 50 and 100 for the SFS metric were the chosen evaluated criteria. Numbers in parenthesis are the corresponding p-values for each coefficient.

4.2.4 SMUS and SFS evaluation

Figure 4.4 shows the SMUS and SFS boxplots for all the delivered plans. According to these graphs, some plans at SMUS 10 and SFS 50 start to get complicated. These thresholds were chosen for further evaluations.

The two different SMUS and SFS criteria correlation coefficients with the plan's total number of segments, MUs, plan's total number of MUs over the total number of segments ratio, and MCS are presented in table 4.7 for all the delivered plans. The SMUS metrics with criteria 10 and 20 have correlations with the total number of MUs, segments, and their ratio, and there were some correlations between the SFS and the MCS values.

Table 4.8 shows the GAI correlation coefficients with SMUS 10 and SFS 50 for two different criteria. All plans together show no correlation with the SMUS or SFS. Site-specific, the HNC GAI has a moderate correlation with SMUS10 and SFS50, and the lung GAI has a weak but significant correlation with SMUS 10. For more metric plots, one can refer to appendix B.

Correlations	3%/3mm vs. SMUS	2%/2mm vs. SMUS	3%/3mm vs. SFS	2%/2mm vs. SFS
Head and Neck	-0.63 (0.02)*	-0.57 (0.04)*	0.35 (0.08)*	0.51 (0.07*)
Liver	0.08 (0.67)	0.08 (0.66)	-0.04 (0.84)	-0.04 (0.83)
Lung	0.29 (0.05)*	0.28 (0.05)*	-0.24 (0.10)	-0.23 (0.11)
Prostate	-0.12 (0.37)	-0.20 (0.14)	-0.14 (0.29)	-0.18 (0.19)
Total	-0.05 (0.60)	-0.08 (0.44)	-0.10 (0.28)	-0.07 (0.49)

Table 4.8: GAI correlation coefficients with SMUS 10 and SFS 50 for all the delivered plans. The values in parenthesis are the corresponding p-values for each coefficient.

Chapter 5

Discussion

Magnetic resonance image guided radiation therapy (MR-linac), a combination of magnetic resonance (MR) imaging and a linear accelerator (Linac) [18] [19], is gaining great interests and is one of the fast growing areas in radiation therapy today. The MR-linac systems enable image guidance with high soft-tissue contrast and daily plan adaptation based on the MR images. However, the target volume daily adaption is only beneficial if combined with a highly conformal delivery technique such as intensity-modulated radiation therapy IMRT or stereotactic body radiation therapy SBRT optimally spare the healthy tissue.

These complex treatment delivery techniques require high accuracy of all machine components and dose delivery verification for each plan. There are several commercial quality assurance QA systems available to perform such verifications on a conventional linear accelerator [48]. However, in consequence of the magnetic field present in the MR-linacs, an MR-compatible QA system is required. But, almost all the conventionally used QA devices, such as ionization chambers, 2D, and 3D detectors arrays, for radiotherapy do not have this characteristic. There are currently few MR-compatible QA systems available.

For example, the Unity Elekta system was evaluated with Farmer ionization chamber [39] [45] [62], EPID images [39] [51] [62], ArcCHECK-MR [45] [62], Octavius 1500 [51], and an MR-compatible prototype of the Delta^4 phantom [53].

Likewise, the MRIdian Viewaray system was previously tested with ionization chambers [40], ArcCHECK-MR [40] [63], Octavius 1500 [63], and Delta^4 + MR phantom [63].

The performance of an adapted MR-compatible Delta^4 phantom device in a 1.5 T MR-linac has been evaluated by De Vries et al. [53]. And, Romaguera et al. have investigated the clinical implementation of the Delta^4+MR phantom on MRIdian systems by measuring the GAI for 14 patients with different treatment sites [63].

But moreover, the purpose of this work was to examine the Delta^4 + MR phantom extensively in a magnetic field of 0.345 T and give a general report on the early clinical experience of using the phantom for patient QA. The basic characteristics of the phantom, such as output stability, dose linearity, field size dependency, angular dependency, and planned versus delivered dose comparisons were examined.

Additionally, three newly defined modulation complexity score (MCS), small monitor unit score (SMUS), and small field score (SFS) metrics were evaluated to determine which treatment plan requires an MR-linac patient-specific QA with the Delta^4 + MR phantom.

5.1 The Delta^4 + MR phantom

The Delta^4 + MR phantom was successfully tested and overall it showed reproducible dose output, good dose linearity, only small field size and angular dependency, and it was suitable for patient-specific QA.

The Delta^4 + MR phantom output deviation was within the clinicaly accepted range and was in agreement with the previous works from De Vries[53] on a 1.5 T MR-Linac and Houweling [45] on a conventional linac.

The relation between the planned dose and the delivered was linear with respect of irradiated MU, but as shown in previous tests from De Vries[53], the lower the number of MUs, the larger the deviation was but the overall deviation is not clinically significant.

All the readings for the gamma evaluation passed the 95% criteria for different field sizes. As the field size increases, so does the difference between the calculated and measured dose value except for the $1.66 \times 1.66\,\mathrm{cm}^2$ field.

The overall gamma passing rate at different gantry angles was more than 95% for the $3\%/3m$ criteria. The largest deviations were detected in 0°, 90°, 180°, and 270°gantry angles due to the plus shape orientation of the detector plates, since the beam enters parallel through the phantom's board at these angles. Similarly, we found that some beams are failing in the patient plans that come from these directions. However the overall plan normally passes which gives us confidence that this is due to a limitation of the phantom. In general, the patient QA results were in agreement with the results from Romaguera's work [63].

The Linac has shown a stable behavior over this time with a good agreement between planned and delivered dose distribution. In the future, the amount of patient-specific measurements on the machine might be reduced and partially replaced by a scoring system for plan complexity combined with a general machine QA to reduce the treatment time.

Throughout the process some limitations were observed. Due to the restricted bore size, some patients cannot be treated with the tumor at the isocenter, therefore, the tumor is often slightly off-center. For these patients the Delta4 dose distribution is also off-center and might fall in between the two arrays. Additionally the analysis is limited by the resolution of the phantom (5 mm in the center and 10 mm outside).

In conclusion, it was shown that the MR compatible phantom is stable over time and shows only a small directional and field size dependence. The Delta^4 + MR phantom can be used for patient-specific QA without any major concerns.

5.2 The MCS, SMUS, and SFS metrics

The introduced MCS, SMUS, and SFS metrics have a fixed range within 0 and 1. They allow a comparison of different treatment sites, alongside the single beam or total treatment plan analysis, on the same scale.

The modulation complexity score has a normal distribution with a 0.38 average. The head and neck plans have the lowest mean of 0.24 since they are the most complicated plans requiring a high precision to minimize the radiation impact on OARs like the spine and the healthy brain tissues. The broadest range of MCS is for lung plans since there are various tumor size and shape in the lung region. The MCS values are smaller than the measured ones for the prostate (0.84), lung (0.63), and head and neck (0.36) on the conventional linac, with a total number of MUs lower than 1100 and segments lower than 100 for each plan [60]. Overall, the treatment plans delivered on the MRIdian system have a higher average total number of MUs (2134) and segments (51) than the ones on the conventional linacs, therefore lower MCS values.

There was no correlation between MCS and the total number of segments, MUs, and MUs over the total number of segments ratio for all the delivered plans. Therefore, MCS can be considered as an independent metric for evaluating treatment plans. However, there was a significant correlation for the IMRT plans, including the liver and head and

neck treatment sites. The correlation between MCS and the total number of segments, MUs, and MUs over the total number of segments ratio was only calculated for the lung plans on the conventional linac, and as the total number of segments and MUs increased, the MCS value decreased [60].

The MCS plots with the total number of segments, MUs, and MUs over the total number of segments ratio for liver and prostate site presented in appendix B show a clustering for each group. The clusters were due to the difference in IMRT and SBRT planning. However, since all the head and neck plans are IMRT and all the lung plans are SBRT, there was no clustering in their plots.

Finally, the MCS and the total number of MUs have no relevant correlation with the GAI for all the delivered plans, which is the same for the measurements on the conventional linac [60], besides the lung and head and neck plans. The absence of correlations can be the result of high GAI values and no failed QAs. And therefore, the machine is delivering the predicted dose accurately for all plans of different complexity levels. The GAI has a better correlation with the total number of MUs than the MCS for these treatment sites. Also, evaluating the total number of MUs for each plan is more feasible in the clinic routine than testing the MCS. In general, the total number of MUs is better for evaluating the complexity of the treatment plans for the lung and head and neck treatment site.

For the SMUS and SFS, the x criteria where the data begins to spread were chosen from the boxplots since they provide the most information for further metric evaluations.

The correlations between these metrics and other features of the plan, such as the MCS and GAI, were only evaluated with the selected criteria from the boxplots.

There was no significant correlation between the SFS metrics with other plan characteristics, except the SFS 50 correlations for the head and neck plans.

On the other hand, there were significant correlations between the SMUS metrics and the total number of MUs, segments, and their ratio. The SMUS metric can provide more information to the QA process, as it is also indicated by the lack of SMUS correlation with the MCS values. Furthermore, there were high SMUS 10 correlations with the GAI values for the lung and head and neck plans, which were even higher than the correlations for the total number of MUs, making SMUS a metric worth further considerations.

The average percentage pass rates for the 3%/3mm criteria was $99.7\% \pm 0.4\%$ and $96.6\% \pm 3.4\%$ for the 2%/2mm for the evaluated treatment plans on the MRIdian, which are higher than the measured values on a conventional linac ($98.7\% \pm 1.0\%$ for the 3%/3mm) [60]. This indicates a generally excellent performance of the MRIdian despite a few failed QAs for the plans with a low number of MUs or small segment areas, which can be why the metrics, except the SMUS, failed.

5.3 Outlook

Further investigations should include QA with a better spatial resolution, such as an EPID imager, which is not yet available for the USZ MRIdian system. Also, some adjustments on the Delta^4 + MR phantom design and software can improve its performance, especially from 0°, 90°, 180°, and 270°angles. Moreover, models predicting the plan complexity can be identified with deep learning or other artificial intelligence methods instead of introducing new complexity modulation metrics.

Bibliography

[1] cancer.org. What is cancer? https://www.cancer.org/content/dam/CRC/PDF/Public/6041.00.pdf. (Accessed on 29.12.2020).

[2] Michel Vert, Yoshiharu Doi, Karl-Heinz Hellwich, Michael Hess, Philip Hodge, Przemyslaw Kubisa, Marguerite Rinaudo, and François Schué. Terminology for biorelated polymers and applications (iupac recommendations 2012). *Pure and Applied Chemistry*, 84(2):377–410, 2012.

[3] John H WEISBURGER. Definition of a carcinogen as a potential human carcinogenic risk. *Japanese Journal of Cancer Research GANN*, 76(12):1244–1246, 1985.

[4] OpenStax. Chemistry. http://cnx.org/contents/85abf193-2bd2-4908-8563-90b8a7ac8df6@9.311., June 2016. (Accessed on 29.12.2020).

[5] Report 16. *Journal of the International Commission on Radiation Units and Measurements*, os9(1):NP–NP, 04 2016.

[6] Harald Paganetti. Proton relative biological effectiveness–uncertainties and opportunities. *International journal of particle therapy*, 5(1):2–14, 2018.

[7] Yoshitaka Matsumoto, Taeko Matsuura, Mami Wada, Yusuke Egashira, Teiji Nishio, and Yoshiya Furusawa. Enhanced radiobiological effects at the distal end of a clinical proton beam: in vitro study. *Journal of radiation research*, 55(4):816–822, 2014.

[8] Ifigeneia V Mavragani, Zacharenia Nikitaki, Spyridon A Kalospyros, and Alexandros G Georgakilas. Ionizing radiation and complex dna damage: From prediction to detection challenges and biological significance. *Cancers*, 11(11):1789, 2019.

[9] Eric J Hall, Amato J Giaccia, et al. *Radiobiology for the Radiologist*, volume 6. Lippincott Williams & Wilkins, 2006.

[10] Z Mansour, Ehab M Attalla, A Sarhan, Ibrahim A Awad, and MI Abdel Hamid. Study the influence of the number of beams on radiotherapy plans for the hyopfractionated treatment of breast cancer using biological model. 2019.

[11] Ben GL Vanneste, Evert J Van Limbergen, Emile N van Lin, Joep GH van Roermund, and Philippe Lambin. Prostate cancer radiation therapy: what do clinicians have to know? *BioMed research international*, 2016, 2016.

[12] Neil G Burnet, Simon J Thomas, Kate E Burton, and Sarah J Jefferies. Defining the tumour and target volumes for radiotherapy. *Cancer Imaging*, 4(2):153, 2004.

[13] Di Yan, Frank Vicini, John Wong, and Alvaro Martinez. Adaptive radiation therapy. *Physics in Medicine & Biology*, 42(1):123, 1997.

[14] SL Morgan-Fletcher. Prescribing, recording and reporting photon beam therapy (supplement to icru report 50), icru report 62., 2001.

[15] Tomas Pavel et al. Feasibility of magnetic resonance imaging-based radiation therapy for brain tumour treatment. 2017.

[16] Nadine Barrie Smith and Andrew Webb. *Introduction to medical imaging: physics, engineering and clinical applications*. Cambridge university press, 2010.

[17] Walter J Curran, David B Hackney, Peter H Blitzer, and Larissa Bilaniuk. The value of magnetic resonance imaging in treatment planning of nasopharyngeal carcinoma. *International Journal of Radiation Oncology* Biology* Physics*, 12(12):2189–2196, 1986.

[18] Jan JW Lagendijk, Bas W Raaymakers, Cornelis AT Van den Berg, Marinus A Moerland, Marielle E Philippens, and Marco Van Vulpen. Mr guidance in radiotherapy. *Physics in Medicine & Biology*, 59(21):R349, 2014.

[19] Marcel van Herk, Alan McWilliam, Michael Dubec, Corinne Faivre-Finn, and Ananya Choudhury. Magnetic resonance imaging–guided radiation therapy: a short strengths, weaknesses, opportunities, and threats analysis. *International Journal of Radiation Oncology• Biology• Physics*, 101(5):1057–1060, 2018.

[20] Slobodan Devic. Mri simulation for radiotherapy treatment planning. *Medical physics*, 39(11):6701–6711, 2012.

[21] J St Aubin, S Steciw, and BG Fallone. Effect of transverse magnetic fields on a simulated in-line 6 mv linac. *Physics in Medicine & Biology*, 55(16):4861, 2010.

[22] AJE Raaijmakers, Bas W Raaymakers, and Jan JW Lagendijk. Integrating a mri scanner with a 6 mv radiotherapy accelerator: dose increase at tissue–air interfaces in a lateral magnetic field due to returning electrons. *Physics in Medicine & Biology*, 50(7):1363, 2005.

[23] AJE Raaijmakers, Björn Hårdemark, Bas W Raaymakers, CPJ Raaijmakers, and Jan JW Lagendijk. Dose optimization for the mri-accelerator: Imrt in the presence of a magnetic field. *Physics in Medicine & Biology*, 52(23):7045, 2007.

[24] J Yun, J St. Aubin, S Rathee, and BG Fallone. Brushed permanent magnet dc mlc motor operation in an external magnetic field. *Medical physics*, 37(5):2131–2134, 2010.

[25] Gary P Liney, B Dong, Jarrad Begg, P Vial, K Zhang, F Lee, A Walker, Roshika Rai, Trent Causer, SJ Alnaghy, et al. Experimental results from a prototype high-field inline mri-linac. *Medical physics*, 43(9):5188–5194, 2016.

[26] Ben Burke, K Wachowicz, BG Fallone, and Satyapal Rathee. Effect of radiation induced current on the quality of mr images in an integrated linac-mr system. *Medical Physics*, 39(10):6139–6147, 2012.

[27] Stan J Hoogcarspel, Stefan E Zijlema, Rob HN Tijssen, Linda GW Kerkmeijer, Ina M Jürgenliemk-Schulz, Jan JW Lagendijk, and Bas W Raaymakers. Characterization of the first rf coil dedicated to 1.5 t mr guided radiotherapy. *Physics in Medicine & Biology*, 63(2):025014, 2018.

[28] Gary P Liney, Bin Dong, Ewald Weber, Robba Rai, Aurelien Destruel, Roberto Garcia-Alvarez, David J Manton, Urszula Jelen, Kevin Zhang, Michael Barton, et al. Imaging performance of a dedicated radiation transparent rf coil on a 1.0 tesla inline mri-linac. *Physics in Medicine & Biology*, 63(13):135005, 2018.

[29] Gary P Liney, B Whelan, B Oborn, Michael Barton, and P Keall. Mri-linear accelerator radiotherapy systems. *Clinical Oncology*, 30(11):686–691, 2018.

[30] Chiara Paganelli, B Whelan, Marta Peroni, Paul Summers, M Fast, Tessa van de Lindt, J McClelland, Björn Eiben, P Keall, T Lomax, et al. Mri-guidance for motion management in external beam radiotherapy: current status and future challenges. *Physics in Medicine & Biology*, 63(22):22TR03, 2018.

[31] Jan JW Lagendijk, Bas W Raaymakers, and Marco Van Vulpen. The magnetic resonance imaging–linac system. In *Seminars in radiation oncology*, volume 24, pages 207–209. Elsevier, 2014.

[32] Sasa Mutic and James F Dempsey. The viewray system: magnetic resonance–guided and controlled radiotherapy, 2014.

[33] Paul J Keall, Michael Barton, Stuart Crozier, et al. The australian magnetic resonance imaging–linac program. In *Seminars in radiation oncology*, volume 24, pages 203–206. Elsevier, 2014.

[34] BG Fallone, B Murray, S Rathee, T Stanescu, S Steciw, S Vidakovic, E Blosser, and D Tymofichuk. First mr images obtained during megavoltage photon irradiation from a prototype integrated linac-mr system. *Medical physics*, 36(6Part1):2084–2088, 2009.

[35] Jan JW Lagendijk, Bas W Raaymakers, Alexander JE Raaijmakers, Johan Overweg, Kevin J Brown, Ellen M Kerkhof, Richard W van der Put, Björn Hårdemark, Marco van Vulpen, and Uulke A van der Heide. Mri/linac integration. *Radiotherapy and Oncology*, 86(1):25–29, 2008.

[36] Jan J.W. Lagendijk, Bas W. Raaymakers, and Marco van Vulpen. The magnetic resonance imaging–linac system, Jun 2014.

[37] BW Raaymakers, IM Jürgenliemk-Schulz, GH Bol, M Glitzner, ANTJ Kotte, B Van Asselen, JCJ De Boer, JJ Bluemink, SL Hackett, MA Moerland, et al. First patients treated with a 1.5 t mri-linac: clinical proof of concept of a high-precision, high-field mri guided radiotherapy treatment. *Physics in Medicine & Biology*, 62(23):L41, 2017.

[38] BW Raaymakers, JJW Lagendijk, J Overweg, JGM Kok, AJE Raaijmakers, EM Kerkhof, RW Van Der Put, I Meijsing, SPM Crijns, F Benedosso, et al. Integrating a 1.5 t mri scanner with a 6 mv accelerator: proof of concept. *Physics in Medicine & Biology*, 54(12):N229, 2009.

[39] I Torres-Xirau, I Olaciregui-Ruiz, G Baldvinsson, BJ Mijnheer, UA Van Der Heide, and A Mans. Characterization of the a-si epid in the unity mr-linac for dosimetric applications. *Physics in Medicine & Biology*, 63(2):025006, 2018.

[40] H Harold Li, Vivian L Rodriguez, Olga L Green, Yanle Hu, Rojano Kashani, H Omar Wooten, Deshan Yang, and Sasa Mutic. Patient-specific quality assurance for the delivery of 60co intensity modulated radiation therapy subject to a 0.35-t lateral magnetic field. *International Journal of Radiation Oncology* Biology* Physics*, 91(1):65–72, 2015.

[41] Ning Wen, Joshua Kim, Anthony Doemer, Carri Glide-Hurst, Indrin J Chetty, Chang Liu, Eric Laugeman, Ilma Xhaferllari, Akila Kumarasiri, James Victoria, et al. Evaluation of a magnetic resonance guided linear accelerator for stereotactic radiosurgery treatment. *Radiotherapy and Oncology*, 127(3):460–466, 2018.

[42] Sebastian Klüter. Technical design and concept of a 0.35 t mr-linac. *Clinical and translational radiation oncology*, 18:98–101, 2019.

[43] X Ronald Zhu, Falk Poenisch, Xiaofei Song, Jennifer L Johnson, George Ciangaru, M Brad Taylor, MingFwu Lii, Craig Martin, Bijan Arjomandy, Andrew K Lee, et al. Patient-specific quality assurance for prostate cancer patients receiving spot scanning proton therapy using single-field uniform dose. *International Journal of Radiation Oncology* Biology* Physics*, 81(2):552–559, 2011.

[44] Sasa Mutic. Patient-specific qa and qa process. https://www.aapm.org/meetings/2014SS/documents/03Tuesday1130-2014AAPMSumerSchool-Mutic-PatientQA-QCforHandout-Final.pdf. (Accessed on 29.12.2020).

[45] AC Houweling, JHW De Vries, J Wolthaus, S Woodings, JGM Kok, B Van Asselen, K Smit, A Bel, JJW Lagendijk, and BW Raaymakers. Performance of a cylindrical diode array for use in a 1.5 t mr-linac. *Physics in Medicine & Biology*, 61(3):N80, 2016.

[46] Danique LJ Barten, Daan Hoffmans, Miguel A Palacios, Stan Heukelom, and Leo J van Battum. Suitability of ebt3 gafchromic film for quality assurance in mr-guided radiotherapy at 0.35 t with and without real-time mr imaging. *Physics in Medicine & Biology*, 63(16):165014, 2018.

[47] Christopher Kurz, Giulia Buizza, Guillaume Landry, Florian Kamp, Moritz Rabe, Chiara Paganelli, Guido Baroni, Michael Reiner, Paul J Keall, Cornelis AT van den Berg, et al. Medical physics challenges in clinical mr-guided radiotherapy. *Radiation Oncology*, 15:1–16, 2020.

[48] Mohammad Hussein, Pejman Rowshanfarzad, Martin A Ebert, Andrew Nisbet, and Catharine H Clark. A comparison of the gamma index analysis in various commercial imrt/vmat qa systems. *Radiotherapy and Oncology*, 109(3):370–376, 2013.

[49] Jochem Kaas, W Van den Wollenberg, AJAJ Van de Schoot, F Wittkämper, and T Janssen. A fast automated sanity check for online plan adaptation in mr-guided rt. In *Radiotherapy and Oncology*, volume 127, pages E553–E554. ELSEVIER IRELAND LTD ELSEVIER HOUSE, BROOKVALE PLAZA, EAST PARK SHANNON, CO ..., 2018.

[50] Luis Alberto Vazquez-Quino, Claudia Ivette Huerta-Hernandez, and Dharanipathy Rangaraj. Clinical experience with machine log file software for volumetric-modulated arc therapy techniques. In *Baylor University Medical Center Proceedings*, volume 30, pages 276–279. Taylor & Francis, 2017.

[51] Iban Torres-Xirau, Igor Olaciregui-Ruiz, Jochem Kaas, Marlies E Nowee, Uulke A van der Heide, and Anton Mans. 3d dosimetric verification of unity mr-linac treatments by portal dosimetry. *Radiotherapy and Oncology*, 146:161–166, 2020.

[52] PTW. Detectors. https://www.ptwdosimetry.com/fileadmin/user_upload/DETECTORS_Cat_en_16522900_12/blaetterkatalog/blaetterkatalog/pdf/complete.pdf. (Accessed on 15.122020).

[53] JHW De Vries, Enrica Seravalli, AC Houweling, Simon J Woodings, Rob van Rooij, Jochem WH Wolthaus, JJW Lagendijk, and Bas W Raaymakers. Characterization of a prototype mr-compatible delta4 qa system in a 1.5 tesla mr-linac. *Physics in Medicine & Biology*, 63(2):02NT02, 2018.

[54] RStudio Team. *RStudio: Integrated Development Environment for R*. RStudio, PBC, Boston, MA, 2020.

[55] Timothy Holmes, Charlie Ma, and Lu Wang. *Monitor Unit*, page 515. Springer Berlin Heidelberg, Berlin, Heidelberg, 2013.

[56] James L Bedford, Young K Lee, Philip Wai, Christopher P South, and Alan P Warrington. Evaluation of the delta4 phantom for imrt and vmat verification. *Physics in Medicine & Biology*, 54(9):N167, 2009.

[57] Daniel A Low, William B Harms, Sasa Mutic, and James A Purdy. A technique for the quantitative evaluation of dose distributions. *Medical physics*, 25(5):656–661, 1998.

[58] Tom Depuydt, Ann Van Esch, and Dominique Pierre Huyskens. A quantitative evaluation of imrt dose distributions: refinement and clinical assessment of the gamma evaluation. *Radiotherapy and oncology*, 62(3):309–319, 2002.

[59] Emiliano Spezi and D Geraint Lewis. Gamma histograms for radiotherapy plan evaluation. *Radiotherapy and oncology*, 79(2):224–230, 2006.

[60] Andrea L McNiven, Michael B Sharpe, and Thomas G Purdie. A new metric for assessing imrt modulation complexity and plan deliverability. *Medical physics*, 37(2):505–515, 2010.

[61] MATLAB. *version 9.9.0.1524771 (R2020b) Update 2*. The MathWorks Inc., 2020.

[62] Xinfeng Chen, Eric S Paulson, Ergun Ahunbay, Aydin Sanli, Slade Klawikowski, and X Allen Li. Measurement validation of treatment planning for a mr-linac. *Journal of applied clinical medical physics*, 20(7):28–38, 2019.

[63] Tino Romaguera. Clinical implementation of delta 4 phantom+ mr for patient-specific qa in 0.35t mr-linac: The miami cancer institute experience.

Appendix A

MATLAB programs

A.1 MCS program and its functions

The *MCS* program calculates the *MCS* for the plan and its beams based on the equations in section MCScalc.

```
for nofield = 1:fieldsNumber

    % ControlPointSequence(CP)
    cpName = fieldnames([Dfile.BeamSequence.(fieldsName{nofield}).
    ControlPointSequence]);
    cpNum  = length(cpName)-1;

    % MU/field
    beamMU(nofield) = Dfile.FractionGroupSequence.Item_1.
    ReferencedBeamSequence.(fieldsName{nofield}).BeamMeterset;

    for noCP = 1:cpNum
        % read MLC position from DICOM file
        MLCleafs  = [Dfile.BeamSequence.(fieldsName{nofield}).
    ControlPointSequence.(cpName{noCP}).BeamLimitingDevicePositionSequence.
    Item_1.LeafJawPositions];

        % adapt MLC position
        [MLCX1,MLCX2] = adaptMLC(MLCleafs);
        % X1,X2 open leaves pair
        [posmax1,posmax2, X1, X2, N]=posmax(MLCX1,MLCX2);
        ...
        % segment area
        area = (MLCX2 - MLCX1)*(4.15);     % half width of each leaf = 4.15
    mm
        areaSeg(noCP,nofield) = sum(area);

        % number of open leaves
        Nn(noCP, nofield)=N;
        LSVs(noCP, nofield)=LSVsegment(posmax1,posmax2, X1, X2, N);

        % MU/segment
        segMU(noCP, nofield) = (Dfile.BeamSequence.(fieldsName{nofield}).
    ControlPointSequence.(cpName{noCP+1}).CumulativeMetersetWeight - ...
            Dfile.BeamSequence.(fieldsName{nofield}).ControlPointSequence.(
    cpName{noCP}).CumulativeMetersetWeight) * ...
            beamMU(nofield);
    end

    for noCP = 1:cpNum
        % read MLC position from DICOM file
```

```
35          MLCleafs  = [Dfile.BeamSequence.(fieldsName{nofield}).
    ControlPointSequence.(cpName{noCP}).BeamLimitingDevicePositionSequence.
    Item_1.LeafJawPositions];
36
37          %adapt MLC position
38          [MLCX1,MLCX2] = adaptMLC(MLCleafs);
39
40          % AAV/segment
41          AAVs(noCP,nofield) = sum(MLCX2-MLCX1)/sum(max(MLC2_all,[],1)-min(
    MLC1_all,[],1));
42      end
43
44      % gantry angle
45      beamAng(nofield) = (Dfile.BeamSequence.(fieldsName{nofield}).
    ControlPointSequence.Item_1.GantryAngle);
46  end
47
48  % MCS and average field size for each beam
49  MCSs(1,fieldsNumber) = zeros;
50  for nofield = 1:fieldsNumber
51      for noCP = 1:cpNum
52          MCSs(1,nofield) = MCSs(1,nofield) + AAVs(noCP,nofield)*LSVs(noCP,
    nofield)*(segMU(noCP,nofield)/beamMU(1,nofield));
53          avgAreaBeam(1,nofield) = mean(areaSeg(:,nofield));
54      end
55  end
56
57  % MCS of the plan
58  MCSplan = sum(MCSs.*(beamMU./sum(beamMU)));
59
60  % average field size of the plan
61  avgAreaPlan = mean(areaSeg,'all');
```

A.1.1 *adaptMLC* function

The *adaptMLC* function sort and adapts MLC positions into left and right MLC bank and stores the coordinates into *MLCX1* and *MLCX2* arrays.

```
1   function [MLCX1, MLCX2] = adaptMLC(MLCleafs)
2
3       % bisect left & right MLC
4       ML = MLCleafs(1:2:end);
5       MR = MLCleafs(2:2:end);
6
7       % left MLC bank
8       for i = 1:length(ML)/2
9           X1(2*i)   = ML(i);
10          X1(2*i-1) = ML(34+i);
11      end
12      X1(69:70) = ML(end);
13      X1(1:6)   = 0;
14      X1(66:70) = 0;
15
16      % right MLC bank
17      for i = 1:length(MR)/2
18          X2(2*i)   = MR(i);
19          X2(2*i-1) = MR(34+i);
20      end
21      X2(69:70) = MR(end);
22      X2(1:6)   = 0;
23      X2(66:70) = 0;
24
25      % compare
```

```
    X1_upper = X1(1:2:end);
    X1_lower = X1(2:2:end);
    X2_upper = X2(1:2:end);
    X2_lower = X2(2:2:end);

    X2adapt(1) = X2_lower(1);
    for i = 1:34
        X2adapt(2*i)   = min(X2_lower(i)  ,X2_upper(i+1));
        X2adapt(2*i+1) = min(X2_lower(i+1),X2_upper(i+1));
    end
    X2adapt(70) = X2_lower(35);
    X1adapt(1) = X1_lower(1);
    for i = 1:34
        X1adapt(2*i)   = max(X1_lower(i)  ,X1_upper(i+1));
        X1adapt(2*i+1) = max(X1_lower(i+1),X1_upper(i+1));
    end
    X1adapt(70) = X1_lower(35);
    for i = 1:70
        if X2adapt(i) < X1adapt(i)
            X2adapt(i) = X1adapt(i);
        end
    end

    % Find closed leafs
    for i = 1:70
        if abs(X1adapt(i)) == abs(X2adapt(i))
        if sign(X1adapt(i)) == sign(X2adapt(i))
            X1adapt(i) = 0;
            X2adapt(i) = 0;
        end
        end
    end

    MLCX1 = X1adapt;
    MLCX2 = X2adapt;
```

A.1.2 *posmax* function

The *posmax* function calculates the *posmax* for each MLC bank based on equation **??** in section MCScalc.

```
function [posmax1, posmax2, X1, X2, N_open] = posmax(MLCX1, MLCX2)

    distMLC = MLCX2-MLCX1;           % contributors (open leaves)
    N_open  = nnz(distMLC);          % number of open leaves
    [row, col_open] = find(distMLC); % col number for open leaves

    if N_open>0
        i=0;
        for j=col_open
            i=i+1;
            X1(i)=MLCX1(j);
            X2(i)=MLCX2(j);
        end
        posmax1=max(X1)-min(X1);
        posmax2=max(X2)-min(X2);
    else
        posmax1=0;
        posmax2=0;
        X1=0;
        X2=0;
    end
```

A.1.3 *LSVsegment* function

The *LSVsegment* function calculates the *LSV* for each segment based on equation 4.1.1 in section MCScalc.

```
function [LSVs] = LSVsegment(posmax1,posmax2, X1, X2, N)

    differ1 = (diff(X1));
    differ2 = (diff(X2));
    sum1    = sum(posmax1-differ1);
    sum2    = sum(posmax2-differ2);

    if posmax1==0
        LB=1;
    elseif N>1
        LB=sum1/((N-1)*posmax1);
    else
        LB=0;
    end
    if posmax2==0
        RB=1;
    elseif N>1
        RB=sum2/((N-1)*posmax2);
    else
        RB=0;
    end

    LSVs = LB*RB;
```

A.1.4 *AAV* function

The *AAV* function calculates the *AAV* for each segment based on equation 4.1.4 in section MCScalc.

```
AAVs(noCP,nofield) = sum(MLCX2-MLCX1)/sum(max(MLC2_all,[],1)-min(MLC1_all
    ,[],1));
```

A.2 SMUS and SFS programs

A.2.1 *MUSxCalc* function

The *MUSxCalc* function calculates the *SMUS* for each segment based on equation 4.1.7 in section smsf.

```
function [MUSx, MUStx] = MUSxCalc(segMU, beamMU, x)

    [nSeg, nBeam] = size(segMU);

    for i = 1:nBeam
        checkSum(i) = 0;
        for j = 1:nSeg
            if segMU(j, i) < x
                checkSum(i) = segMU(j, i) + checkSum(i);
            end
        end
        MUSx(i) = 1 - checkSum(i)/beamMU(i);
    end

    MUStx = 1 - sum(checkSum(:))/sum(beamMU(:));
```

A.2.2 *SFSxCalc* function

The *SFSxCalc* function calculates the *SFS* for each segment based on equation 4.1.9 in section smsf.

```
function [SFSx, SFStx] = SFSxCalc(segMU, segSurf, beamMU, x)

    [nSeg, nBeam] = size(segMU);

    for i = 1:nBeam
        checkSum(i) = 0;
        for j = 1:nSeg
            if abs(segSurf(j, i)) < x
                checkSum(i) = segMU(j, i) + checkSum(i);
            end
        end
        SFSx(i) = 1 - checkSum(i)/beamMU(i);
    end

    SFStx = 1 - sum(checkSum(:))/sum(beamMU(:));
```

Appendix B

MSC, SMUS, and SFS metrics

The MCS values were plotted versus different plan features with a linear regression model with equation 4.1.11, where x can be the plan's total number of segments, the total number of MUs, or the total number of MUs over the total number of segments ratio for each treatment site.

x	p_1	p_2	R^2	Correlation coefficient
#segments	-152.61	123.91	0.50	-0.71
#MU	-2949.5	1637	0.76	-0.87
#MU/#segments	-15.22	14.23	0.46	-0.68

Table B.1: Linear regression and correlation coefficients for the head and neck plans

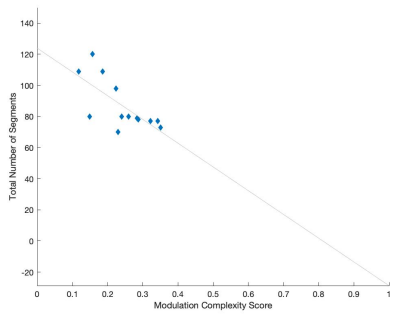

(a) Number of segments vs. MCS

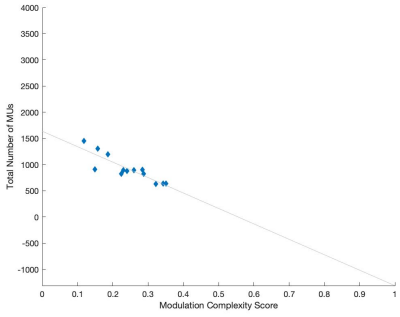

(b) Number of MUs vs. MCS

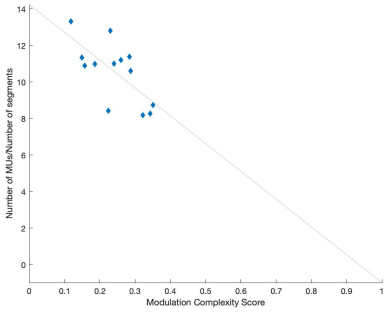

(c) Number of MU/segments vs. MCS

Figure B.1: MCS relation with the total number of segments, MUs, and MUs over the total number of segments for the head and neck delivered plans.

x	p_1	p_2	R^2	Correlation coefficient
#segments	40.16	36.71	0.20	0.45
#MU	-2108.40	2382	0.08	-0.28
#MU/#segments	-56.09	52.18	0.15	-0.39

Table B.2: Linear regression and correlation coefficients for the liver plans

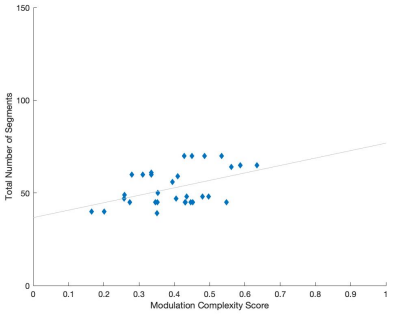

(a) Number of segments vs. MCS

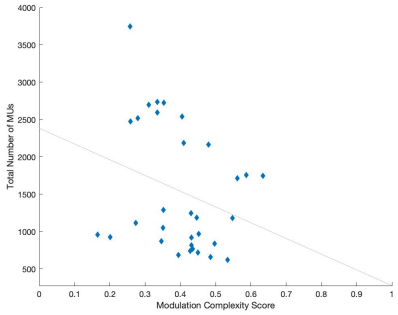

(b) Number of MUs vs. MCS

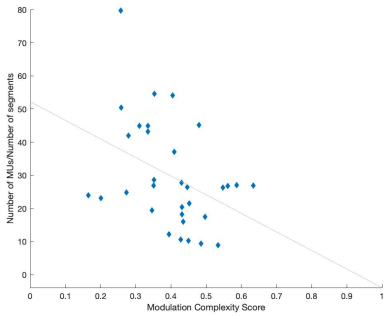

(c) Number of MU/segments vs. MCS

Figure B.2: MCS relation with the total number of segments, MUs, and MUs over the total number of segments for the liver delivered plans.

x	p_1	p_2	R^2	Correlation coefficient
#segments	-22.56	34.56	0.11	-0.34
#MU	457.56	2942	0.01	0.06
#MU/#segments	125.49	88.58	0.08	0.29

Table B.3: Linear regression and correlation coefficients for the lung plans

x	p_1	p_2	R^2	Correlation coefficient
#segments	23.37	46.16	0.05	0.22
#MU	578.69	1637	0.01	0.07
#MU/#segments	-12.94	40.25	0.01	-0.05

Table B.4: Linear regression and correlation coefficients for the prostate plans

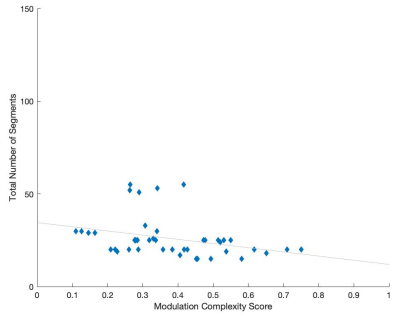

(a) Number of segments vs. MCS

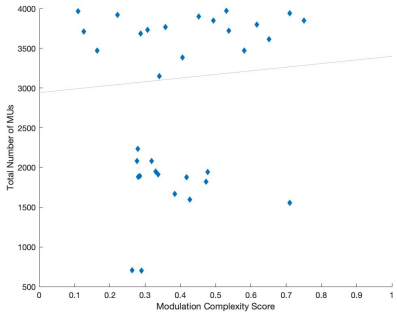

(b) Number of MUs vs. MCS

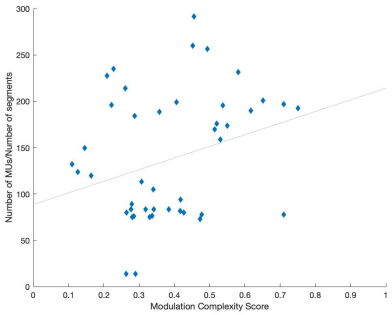

(c) Number of MU/segments vs. MCS

Figure B.3: MCS relation with the total number of segments, MUs, and MUs over the total number of segments for the lung delivered plans.

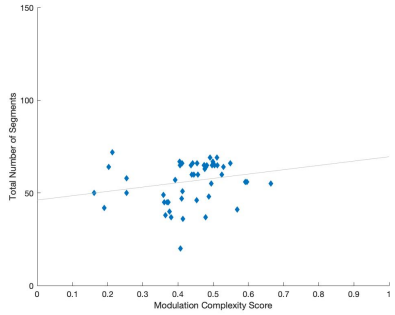

(a) Number of segments vs. MCS

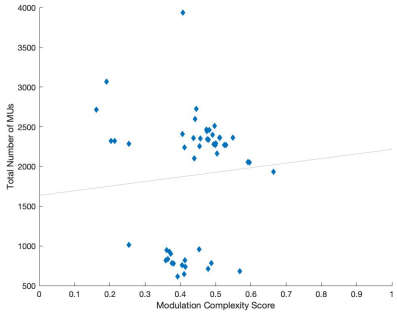

(b) Number of MUs vs. MCS

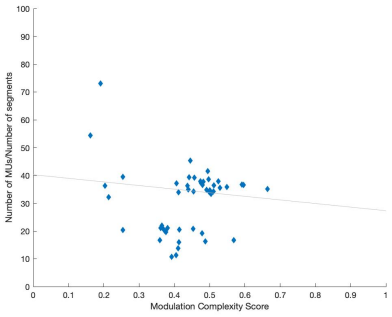

(c) Number of MU/segments vs. MCS

Figure B.4: MCS relation with the total number of segments, MUs, and MUs over the total number of segments for the prostate delivered plans.

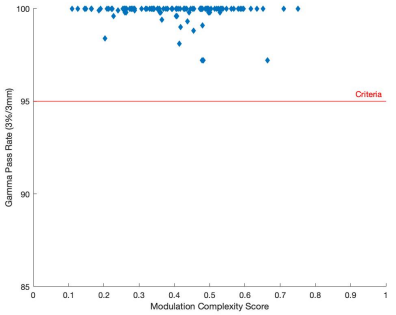

(a) 3%/3mm GAI vs. MCS

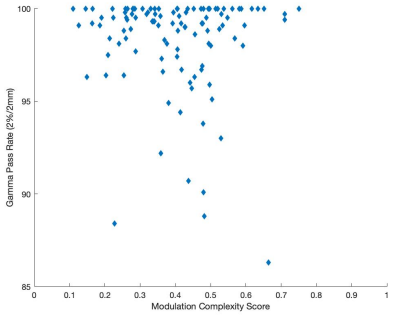

(b) 2%/2mm GAI vs. MCS

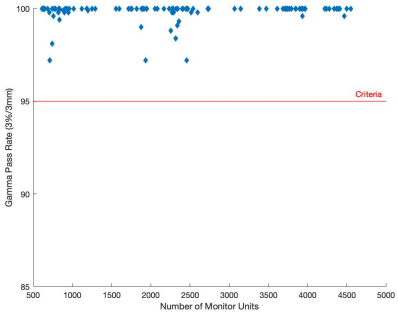

(c) 3%/3mm GAI vs. #MUs

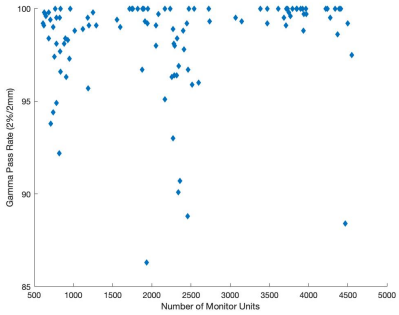

(d) 2%/2mm GAI vs. #MUs

Figure B.5: GAI relation with the MCS and total number of MUs for all the delivered plans. The red line is the 95% acceptance rate for GAI with 3%/3mm criteria.

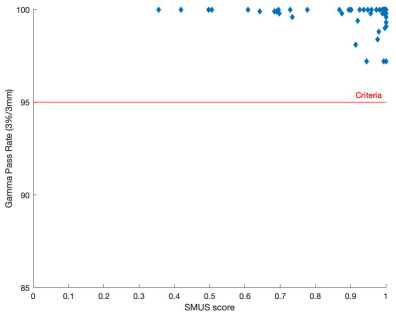

(a) 3%/3mm GAI vs. SMUS

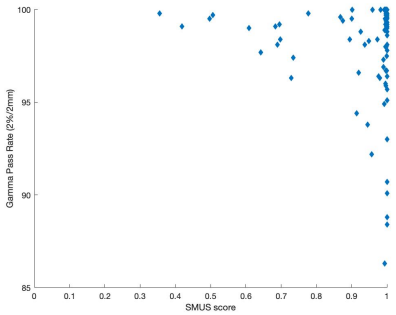

(b) 2%/2mm GAI vs. SMUS

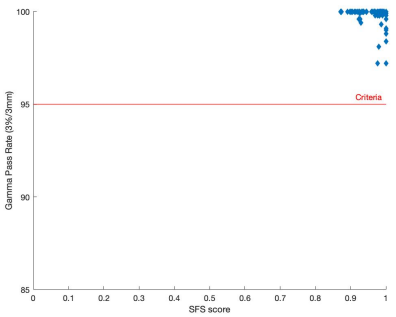

(c) 3%/3mm GAI vs. SFS

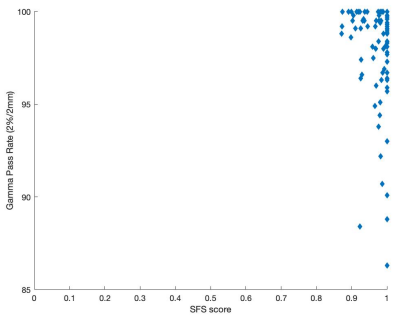

(d) 2%/2mm GAI vs. SFS

Figure B.6: GAI relation with the SMUS 10 and SFS 50 for all the delivered plans. The red line is the 95% acceptance rate for GAI with 3%/3mm criteria.

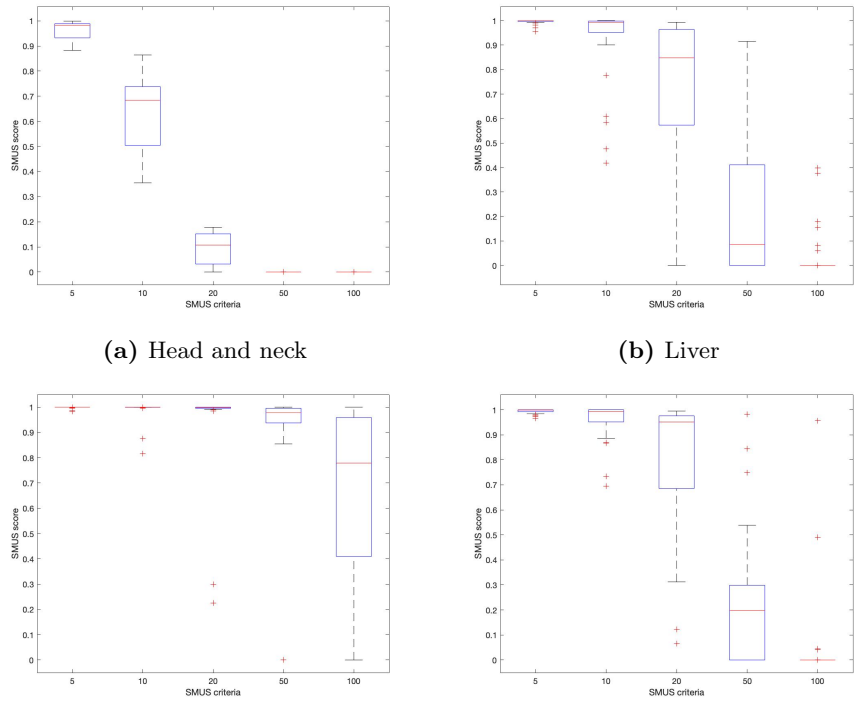

(a) Head and neck **(b)** Liver

(c) Lung **(d)** Prostate

Figure B.7: SMUS boxplot with criteria 5, 10, 20, 50, and 100 for each treatment site. The x-axis for SMUS metric is the total number of MUs per segment.

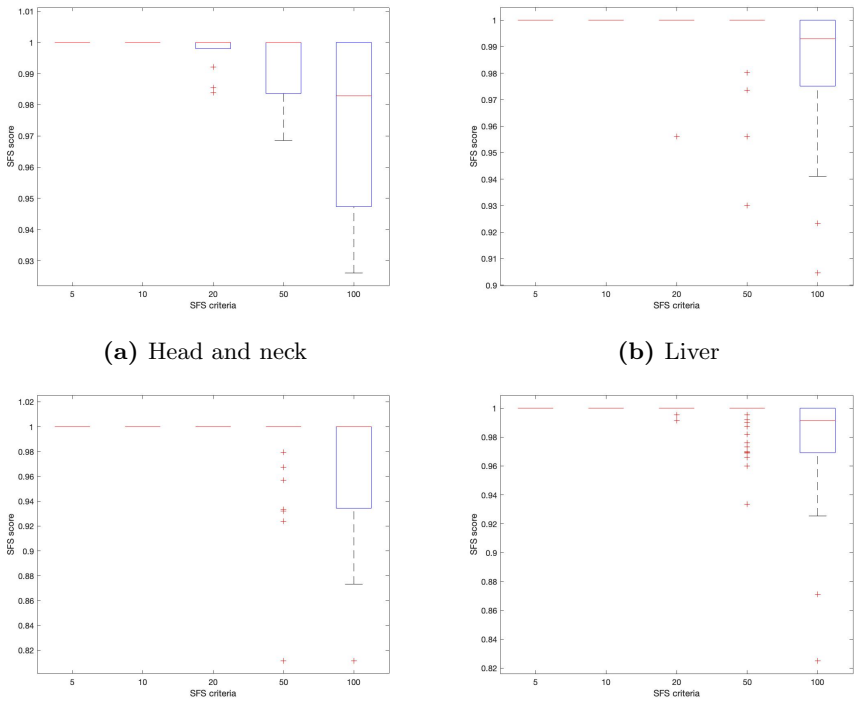

(a) Head and neck **(b)** Liver

(c) Lung **(d)** Prostate

Figure B.8: SFS boxplot with criteria 5, 10, 20, 50, and 100 for each treatment site. The x-axis for SFS is segment area in mm^2.